Grant Agreement: 825027

Start date: 01.01.2019

Duration: 44 months

AD ASTRA Deliverable D5.3

"Final version of performance and RUL prediction models including Probabilistic degradation functions with validated accelerating factors and multiple model prognosis"

Due date of deliverable: M44

Lead Beneficiary: UNIGE

Nature: Report

Revision	Submission date	Description
1	1/08/2022	Work scheme
2	1/09/2022	First draft from each partner
3	12/09/2022	First full draft
4	10/10/2022	Final manuscript to be submitted

Dissemination level (mark with an x the relevant)		
PU	Public	**x**
CO	Confidential, only for members of the consortium (including the Commission Services)	

Acknowledgements: This project has received funding from the Fuel Cells and Hydrogen 2 Joint Undertaking (now Clean Hydrogen Partnership) under Grant Agreement No 825027. This

Joint Undertaking receives support from the European Union's Horizon 2020 Research and Innovation program, Hydrogen Europe and Hydrogen Europe Research.

Report title: "Final version of performance and RUL prediction models including Probabilistic degradation functions with validated accelerating factors and multiple model prognosis"	**Deliverable No. D5.3**
Responsible author: Barbara Bosio (UNIGE)	
Authors: **Jerome Laurencin (CEA), Fiammetta Bianchi (UNIGE), Pierpaolo Polverino (UNISA), Cesare Pianese (UNISA), Alfonso Pandolfi (UNISA), Aline Leon (EIFER), Christoph Kändler (EIFER)**	

Summary

Modelling activity has a central role in studies on solid oxide cells allowing for a more concrete understanding of mechanisms and underlining the correlations among several factors which can influence the cell operation such as materials, geometry, microstructure and working conditions. Here model results provide a useful guide to improve cell behaviour in order to make this technology competitive for long-lasting applications as both power plant and energy storage unit. In the framework of AD ASTRA project different approaches have been proposed as performance and lifetime models consisting in lumped-parameter models, high level physics-based models, statistic models and signal-based learning model. They can be successfully used for different purposes as listed below:

- cell operation analysis in view of specific kinetics occurred in each electrode;
- cell performance prediction at nominal state and during operation;
- degradation accelerating factor identification and transfer functions for their correlation to cell operation;
- cell prognosis in term of Remaining Useful Life (RUL).

Key words: Solid oxide cell, Multiscale modelling, Performance prediction, Remaining useful life, Degradation functions, Transfer functions.

TABLE OF CONTENT

Introduction

Modelling activity has a central role in studies on solid oxide cells allowing for a more concrete understanding of mechanisms and underlining the correlations among several factors which influence the cell operation such as materials, geometry, microstructure and working conditions. Here model results provide a useful guide to improve cell behaviour in order to make this technology competitive for long-lasting applications as both power plant and energy storage unit. In the framework of AD ASTRA project, different approaches have been proposed as performance and lifetime models to simulate how the cells work during durability and accelerated stress tests. Indeed, both empirical and physics-based degradation functions have been introduced deriving them from experimental observations, specific high-level and grey-box degradation models. Remaining Useful Life (RUL) can be predicted in order to organise properly maintenance before a complete irreversible failure of cells. Moreover, degradation accelerating factors have been also correlated to cell operation through specific transfer functions aiming at the detection of parameters which mainly cause the worsening of performance.
Following sections present a detailed description of models developed within AD ASTRA consortium.

I. Local level models for cell kinetics analysis and degradation (CEA)

Main CEA task consisted in developing micro-scale models to study the Ni-YSZ and LSCF electrode kinetics and degradation, which represent the state-of-art materials for solid oxide cells.

I.1 Developments for the Ni-YSZ fuel electrode

Electrochemical modelling to study the impact of Ni coarsening and migration

A model-based double-hydrogen spillover mechanism has been chosen and implemented in a Finite Element code in order to analyse the Ni coarsening and migration arising upon operation. The global reaction pathway for this particular model is depicted in Figure I.1, while the reactions and their kinetic rates are listed in Table I.1. The details for all the governing equations can be found in reference [1].

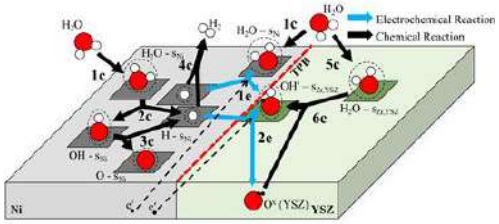

Figure I.1 Elementary reactions taken into account in the fuel electrode kinetic model to analyse the impact of Ni coarsening and migration.

Table I.1 Elementary electrochemical reactions considered in the microscale model for Ni-YSZ fuel electrode.

Reaction		Kinetics
1c	$H_2O(gas)+s_{Ni} \underset{k^{des}_{H_2O,Ni}}{\overset{k^{ads}_{H_2O,Ni}}{\rightleftarrows}} H_2O\text{-}s_{Ni}$	$v^{ads}_{H_2O,Ni}=Sp_{p\text{-}Ni}\cdot\Gamma_{Ni}\cdot\left(k^{ads}_{H_2O,Ni}\cdot\frac{p(H_2O)}{p_{ref}}\cdot\theta_{s_{Ni}}-k^{des}_{H_2O,Ni}\cdot\theta_{H_2O_{Ni}}\right)$
2c	$H_2O\text{-}s_{Ni}+s_{Ni} \underset{k^{ass}_{H_2O,Ni}}{\overset{k^{diss}_{H_2O,Ni}}{\rightleftarrows}} H\text{-}s_{Ni}+OH\text{-}s_{Ni}$	$v^{diss}_{H_2O,Ni}=Sp_{p\text{-}Ni}\cdot\Gamma^2_{Ni}\cdot\left(k^{diss}_{H_2O,Ni}\cdot\theta_{H_2O_{Ni}}\cdot\theta_{s_{Ni}}-k^{ass}_{H_2O,Ni}\cdot\theta_{H_{Ni}}\cdot\theta_{OH_{Ni}}\right)$
3c	$OH\text{-}s_{Ni}+s_{Ni} \underset{k^{ass}_{OH,Ni}}{\overset{k^{diss}_{OH,Ni}}{\rightleftarrows}} H\text{-}s_{Ni}+O\text{-}s_{Ni}$	$v^{diss}_{OH,Ni}=Sp_{p\text{-}Ni}\cdot\Gamma^2_{Ni}\cdot\left(k^{diss}_{OH,Ni}\cdot\theta_{OH_{Ni}}\cdot\theta_{s_{Ni}}-k^{ass}_{OH,Ni}\cdot\theta_{O_{Ni}}\cdot\theta_{H_{Ni}}\right)$
4c	$2H\text{-}s_{Ni} \underset{k^{ads}_{H_2,Ni}}{\overset{k^{des}_{H_2,Ni}}{\rightleftarrows}} H_2(gas)+2s_{Ni}$	$v^{des}_{H_2,Ni}=Sp_{p\text{-}Ni}\cdot\Gamma^2_{Ni}\cdot\left(k^{des}_{H_2,Ni}\cdot\theta^2_{H_{Ni}}-k^{ads}_{H_2,Ni}\cdot\frac{p(H_2)}{p_{ref}}\cdot\theta^2_{s_{Ni}}\right)$
5c	$H_2O(gas)+s_{Zr,YSZ} \underset{k^{des}_{H_2O,YSZ}}{\overset{k^{ads}_{H_2O,YSZ}}{\rightleftarrows}} H_2O\text{-}s_{Zr,YSZ}$	$v^{ads}_{H_2O,YSZ}=Sp_{p\text{-}YSZ}\cdot\Gamma_{YSZ}\cdot\left(k^{ads}_{H_2O,YSZ}\cdot\frac{p(H_2O)}{p_{ref}}\cdot\theta_{s_{Zr}}-k^{des}_{H_2O,YSZ}\cdot\theta_{H_2O_{Zr}}\right)$
6c	$H_2O\text{-}s_{Zr,YSZ}+O^{x}_{O}(YSZ)+s_{Zr,YSZ} \underset{k^{ass}_{H_2O,YSZ}}{\overset{k^{diss}_{H_2O,YSZ}}{\rightleftarrows}} 2OH^{'}\text{-}s_{Zr,YSZ}+V^{\cdot\cdot}_{O}(YSZ)$	$v^{diss}_{H_2O,YSZ}=Sp_{p\text{-}YSZ}\cdot\Gamma^2_{YSZ}\cdot\left(k^{diss}_{H_2O,YSZ}\cdot\theta_{H_2O_{Zr}}\cdot\theta_{s_{Zr}}-k^{ass}_{H_2O,YSZ}\cdot\theta^2_{OH^{'}_{Zr}}\right)$
1e	$H_2O\text{-}s_{Ni}+s_{Zr,YSZ}+1e^{'}_{Ni} \underset{k^{ox}_{ct_1}}{\overset{k^{red}_{ct_1}}{\rightleftarrows}} OH^{'}\text{-}s_{Zr,YSZ}+H\text{-}s_{Ni}$	$v^{red}_{ct_1}=\xi_{TPBls}\cdot\Gamma_{Ni}\cdot\Gamma_{YSZ}\cdot\left(k^{red}_{ct_1}\cdot\theta_{H_2O_{Ni}}\cdot\theta_{s_{Zr}}\cdot\exp\left(\frac{-\alpha^{red}_{ct_1}F}{RT}\eta\right)-k^{ox}_{ct_1}\cdot\theta_{H_{Ni}}\cdot\theta_{OH^{'}_{Zr}}\cdot\exp\left(\frac{\alpha^{ox}_{ct_1}F}{RT}\eta\right)\right)$
2e	$OH^{'}\text{-}s_{Zr,YSZ}+V^{\cdot\cdot}_{O}(YSZ)+s_{Ni}+1e^{'}_{Ni} \underset{k^{ox}_{ct_2}}{\overset{k^{red}_{ct_2}}{\rightleftarrows}} H\text{-}s_{Ni}+O^{x}_{O}(YSZ)+s_{Zr,YSZ}$	$v^{red}_{ct_2}=\xi_{TPBls}\cdot\Gamma_{Ni}\cdot\Gamma_{YSZ}\cdot\left(k^{red}_{ct_2}\cdot\theta_{OH^{'}_{Zr}}\cdot\theta_{s_{Ni}}\cdot\exp\left(\frac{-\alpha^{red}_{ct_2}F}{RT}\eta\right)-k^{ox}_{ct_2}\cdot\theta_{H_{Ni}}\cdot\theta_{s_{Zr}}\cdot\exp\left(\frac{\alpha^{ox}_{ct_2}F}{RT}\eta\right)\right)$

It is worth noting that the model was validated on specific electrochemical measurements performed on the Ni-YSZ cermet of the SOLIDpower cell [1]. To reduce the number of unknown parameters for the simulations, the real microstructural properties of the tested cermet have been deduced from a 3D electrode reconstruction obtained by synchrotron X- ray nano-holotomography. It has been shown that the model based on the hydrogen spillover mechanism is able to correctly predict the electrode response in terms of impedance spectra and polarization curves obtained at different gas compositions (Figure I.2). Once validated, the model based on the hydrogen spillover mechanism has been used to clarify the reaction pathway for the Ni-3YSZ electrode. The analysis of the

simulated impedance diagrams at Open Circuit Potential (OCP) has confirmed that the rate determining steps are (i) the charge transfer at TPBIs, (ii) the oxygen vacancies migration in YSZ network and (iii) a pure chemical surface process. Moreover, the simulations under polarizations have highlighted a change of reaction pathway from cathodic to anodic polarization.

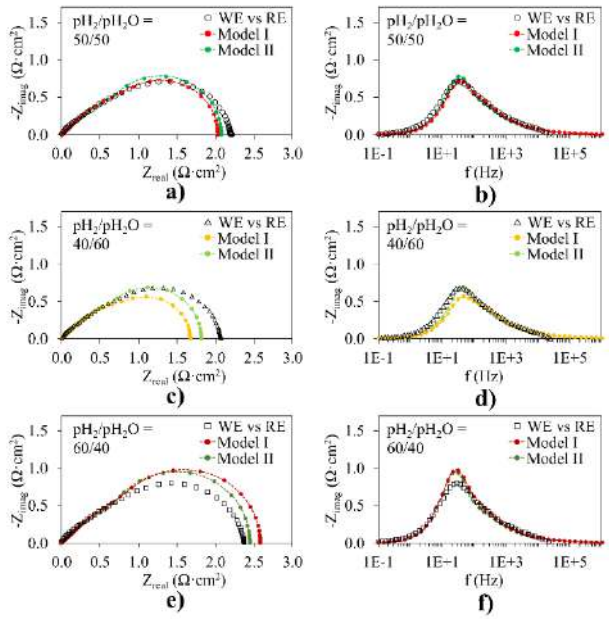

Figure I.2 Experimental and simulated impedance spectra at OCP with different pH_2/pH_2O: Nyquist (a) and Bode (b) plots with pH_2/pH_2O = 50/50 – Nyquist (c) and Bode (d) plots with pH_2/pH_2O = 40/60 – Nyquist (e) and Bode (f) plots with pH_2/pH_2O = 60/40 [1].

Once validated, the model was used to study the impact of Ni coarsening and migration using SOLIDpower cells. All the results are detailed in reference [2]. In this study, the hydrogen electrodes of pristine and aged cells have also been reconstructed by synchrotron X-ray holotomography. Thanks to the large volume of the 3D images, the Ni-YSZ microstructural evolutions have been investigated in the bulk and at the electrode/electrolyte interface. The quantification of the microstructural properties in the bulk has revealed a Ni particle growth for all the operated samples. This phenomenon of agglomeration was found to be independent of the polarization. The microstructural evolutions have been introduced in the model to quantify the impact of the Ni agglomeration on the electrode and cell performances. Thanks to the data extracted from the longest experimental dataset, the effects of the Ni agglomeration have been extrapolated up to 20,000 hours with a good level of confidence (Figure I.3). As expected, the contribution of the agglomeration on the cell degradation is significant but tends to slow down for very long-term operation.

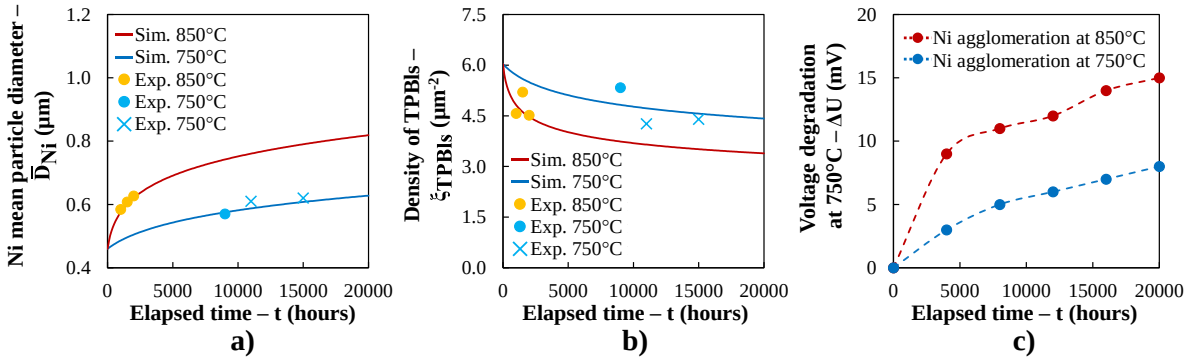

Figure I.3 Effects of the hydrogen electrode microstructural evolution on the electrode and cell performances: Increase of the Ni mean particle diameter associated to the Ni agglomeration (a) – Effect of the Ni agglomeration on the density of TPBls (b) – Simulated voltage caused by Ni agglomeration at 750 °C and 850 °C drop assuming cell operation at 750 °C and -0.5 A.cm^{-2} for this comparison (c) [2].

The analyses of the 3D electrode reconstructions have also revealed a Ni migration toward the bulk of the electrodes resulting in Ni depletion at the electrode/electrolyte interfaces for the cells operated in electrolysis mode. As for the agglomeration, the gradients in microstructure parameters due to the loss of Ni at the electrode/electrolyte interface have been implemented in the model. The effect of the Ni depletion on the polarisation curve and impedance spectra have been also computed and discussed. It has been shown that the Ni depletion can represent a large part of the degradation in electrolysis mode.

Mechanical modelling to study the impact of Ni re-oxidation

An original model based on the phase field approach has been developed to study the local fracture in porous electrodes of Solid Oxide Cells (SOCs). First, the model capacity to predict the crack nucleation and propagation has been studied with theoretical considerations which are detailed in reference [3]. Then, the model was validated thanks to performed specific micro-compression tests. It has been found that the model is able to simulate accurately the YSZ compressive fracture strength as a function of porosity (Figure I.4). Moreover, it has been shown that the model is able to capture and explain the transition from a brittle behavior towards a diffuse damage when increasing the porosity [3].

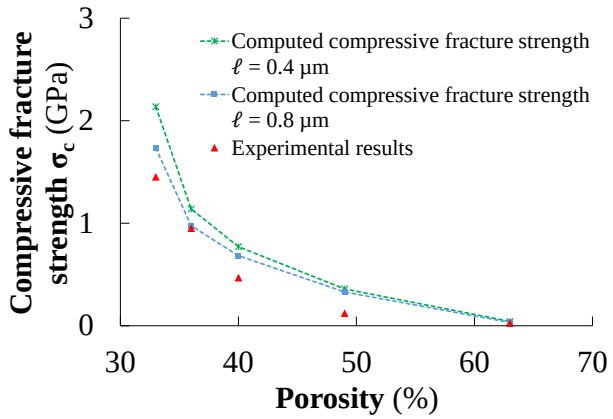

Figure I.4 Comparison between the calculated compressive fracture strength and the experimental data as a function of porosity, where l is the regularization parameter in the phase-field simulation.

After its validation, the model has been used to study the impact of Ni re-oxidation [4,5]. As expected, it has been found that the Ni swelling during the Ni-NiO transformation induces a mechanical damage in the YSZ backbone of the electrode (Figure I.5). It has been found that the micro-cracks are generated into the YSZ ligaments surrounded by Ni with specific morphological characteristics and submitted to high tensile stresses during the re-oxidation. In addition, the comparison between the investigated microstructures of two typical cermet supports (Ni-3YSZ and Ni-8YSZ) has confirmed the crucial role of the YSZ backbone (Figure I.5). Indeed, the local fracture of the YSZ skeleton and the number of the created micro-cracks are strongly dependent on the fracture properties of the ceramic. As expected, it has been found that the Ni-3YSZ cermet has a higher redox tolerance with respect to Ni-8YSZ. Moreover, it has been also shown that the microstructural properties of the cermet can also play a role on the cermet mechanical stability. As observed during experiments, the microstructure with higher porosity and smaller Ni particles provides higher mechanical stability upon the Ni re-oxidation with the formation of less micro-cracks [5].

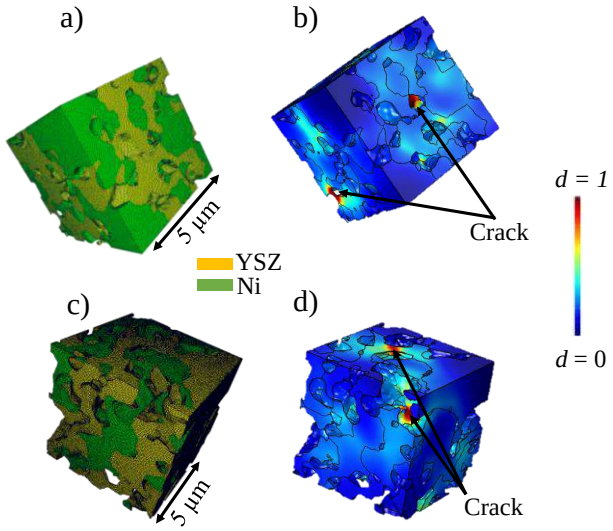

Figure I.5 Finite Element meshes of the simulated solid phases in the Ni-YSZ volumes of 5x5x5 µm³: (a) Ni-8YSZ, and (c) Ni-3YSZ. Micro-cracks simulated with the model during re-oxidation in (b) Ni-8YSZ and (d) Ni-3YSZ [5].

I.2 Developments for the LSCF air electrode

An elementary kinetic model has been also developed to study the impact of the LSCF decomposition on electrode performances. The two reaction pathways implemented in the model are shown in Figure I.6. The associated reactions and their kinetic rates are provided in Table I.2. The details for all the governing equations can be found in reference [6].

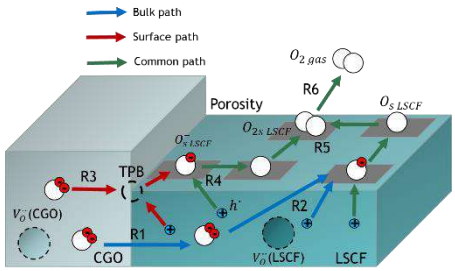

Figure I.6 Elementary reactions taken into account in the air electrode kinetic model to analyse the impact of LSCF demixing [6].

Table I.2 Reactions and expressions of the kinetic rates for LSCF air electrode.

Reaction		Kinetics
R1	$\underset{k_-}{\overset{k_+}{\leftrightarrow}}\ O_O^x(CGO) + V_o^{\cdot\cdot}(LSCF) \leftrightarrow O_O^x(LSCF) + V_o^{\cdot\cdot}(CGO)$	$\nu_{(1)} = S_p^{CGO/LSCF}\left\{k_+ exp\left(\frac{2\alpha_{(1)}^{ox}FE}{RT}\right)\left(\frac{C_{V_O}}{C_{O_O^x}^{max}}\right) - k_- exp\left(\frac{-2\alpha_{(1)}^{red}FE}{RT}\right)\left(\frac{C_{O_O^x}^{max} - C_{V_O}}{C_{O_O^x}^{max}}\right)\right\}$
R2	$\underset{k_{red}^{LSCF/gas}}{\overset{k_{ox}^{LSCF/gas}}{\leftrightarrow}}\ O_O^x(LSCF) + 1h^{\cdot} + 1s_{LSCF} \leftrightarrow V_o^{\cdot\cdot}(LSCF) + O^- - s_{LSCF}$	$\nu_{(2)} = S_p^{LSCF/gas}\left\{k_{ox}^{LSCF/gas} exp\left(\frac{\alpha_{(2)}^{ox}F\chi}{RT}\right)((C_{O_O^x}^{max} - C_{V_O^{\cdot\cdot}})\Gamma\theta_{s_{LSCF}}) - k_{red}^{LSCF/gas} exp\left(\frac{-\alpha_{(2)}^{red}F\chi}{RT}\right)(\Gamma\theta_{O^- - s_{LSCF}}C_{V_O^{\cdot\cdot}})\right\}$
R3	$\underset{k_{red}^{TPBls}}{\overset{k_{ox}^{TPBls}}{\leftrightarrow}}\ O_O^x(CGO) + 1h^{\cdot} + 1s_{LSCF} \leftrightarrow O^- - s_{LSCF} + V_o^{\cdot\cdot}(CGO)$	$\nu_{(3)} = \xi_{TPBs}\left\{k_{ox}^{TPBls} exp\left(\frac{\alpha_{(3)}^{ox}FE}{RT}\right)\Gamma\theta_{s_{LSCF}} - k_{red}^{TPBls} exp\left(\frac{-\alpha_{(3)}^{red}FE}{RT}\right)\Gamma\theta_{O^- - s_{LSCF}}\right\}$
R4	$\underset{k_{ion}}{\overset{k_{deion}}{\leftrightarrow}}\ O^- - s_{LSCF} + 1h^{\cdot} \leftrightarrow O - s_{LSCF}$	$\nu_{(4)} = S_p^{LSCF/gas}\left\{k_{deion} exp\left(\frac{\alpha_{(4)}^{ox}F\chi}{RT}\right)(\Gamma\theta_{O^- - s_{LSCF}}) - k_{ion} exp\left(\frac{-\alpha_{(4)}^{red}F\chi}{RT}\right)(\Gamma\theta_{O - s_{LSCF}})\right\}$
R5	$\underset{k_{diss}}{\overset{k_{ass}}{\leftrightarrow}}\ 2O - s_{LSCF} \leftrightarrow O_2 - s_{LSCF} + 1s_{LSCF}$	$\nu_{(5)} = S_p^{LSCF/gas}\left\{k_{ass}\Gamma^2\theta_{O - s_{LSCF}}{}^2 - k_{diss}\Gamma^2\theta_{O_2 - s_{LSCF}}\theta_{s_{LSCF}}\right\}$
R6	$\underset{k_{ads}}{\overset{k_{des}}{\leftrightarrow}}\ O_2 - s_{LSCF} \leftrightarrow O_2(gas) + 1s_{LSCF}$	$\nu_{(6)} = S_p^{LSCF/gas}\left\{k_{des}\Gamma\theta_{O_2 - s_{LSCF}} - k_{ads}P_{O_2}\Gamma\theta_{s_{LSCF}}\right\}$

The model was validated thanks to experiments performed on symmetrical cells using a three-electrode setup. After the model calibration on polarization curves, it has been shown that the model is able to simulate accurately the experimental impedance diagram at OCP and under polarization without additional fitting. Moreover, the evolution of the electrode polarization resistance with the oxygen partial pressure is well reproduced by the model. The electrode reaction mechanism was thoroughly analysed depending on the electrode polarisation mode in SOFC and SOEC [6].
The impact of the perovskite decomposition on the LSCF electrode response has been studied with the model at OCP and under anodic and cathodic dc currents [6]. The surface passivation and the loss of ionic conductivity have been simulated by decreasing the specific surface area and the chemical diffusivity, respectively (Figure I.7). At OCV, the impact of the demixing on the evolution of the impedance spectra has been discussed. It has been shown that the passivation affects the contribution at low frequency in the Gerisher-type element, while the loss of ionic conductivity enlarges the contribution at intermediate frequency.
It has been stated that the surface passivation is more affecting the electrode response when the performances are evaluated under electrolysis mode. On the contrary, the electrode polarization resistance is more sensitive to the decrease of ionic conductivity when the response is evaluated in fuel cell mode. Finally, whatever the conditions, it appears that the surface passivation would be more impacting than the decrease of the ionic conductivity. Moreover, the sum of the degradation induced by the two phenomena is higher when the electrode response is computed in anodic polarization. Therefore, the LSCF decomposition would be more detrimental for the electrode performances in electrolysis mode.

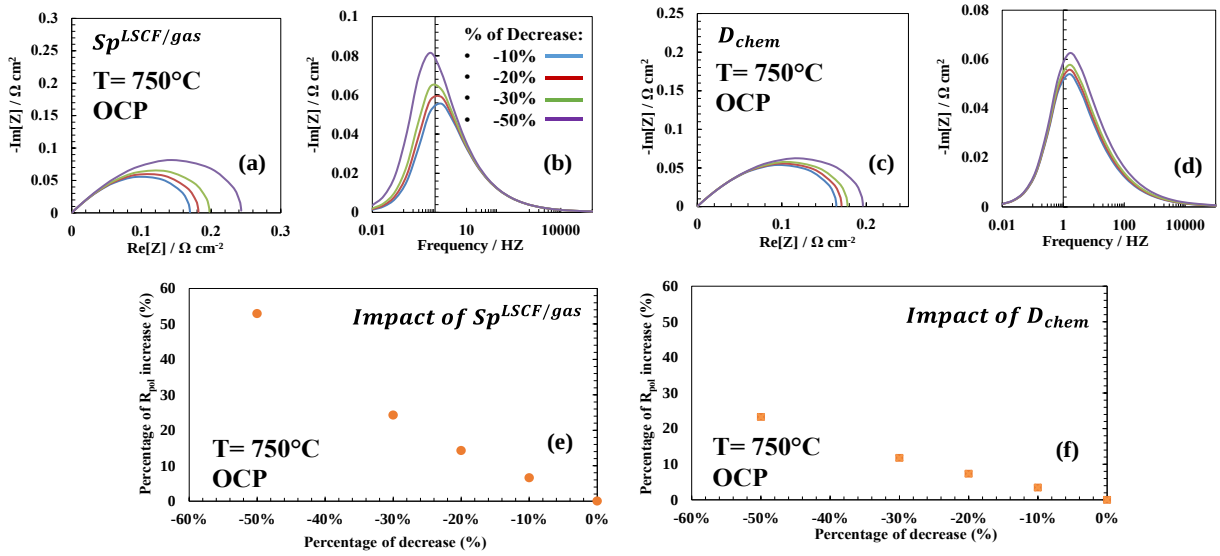

Figure I.7 Sensitivity analysis on the surface passivation and on the loss of ionic conductivity at 750 °C under air at OCP: Nyquist and Bode plots evolution (a) and (b) for the surface passivation, (c) and (d) for the loss of ionic conductivity, respectively. Evolution of the polarization resistance with the decrease of (e) the specific surface area and of (f) the chemical diffusivity.

The model was finally extended and validated to simulate the LSCF cyclic voltammetry response [7,8]. It has been also shown that the voltammograms are strongly distorted by the Ohmic losses making their interpretation impossible in practice under the classical operating conditions of the solid oxide cells. To overcome this limitation, a methodology based on our modelling approach has been proposed to remove the Ohmic losses from the voltammograms and hence to reveal the voltammetry peaks. Thanks to this procedure, the impact of the LSCF decomposition on the cyclic voltammetry response has been estimated with model. It has been established that the surface passivation and the decrease of the chemical diffusivity can substantially affect the shape of the voltammograms. Therefore, the cyclic voltammetry could be seen as a relevant alternative method to characterize the electrode degradation.

REFERENCES

[1] F. Monaco, E. Effori, M. Hubert, E. Siebert, G. Geneste, B. Morel, E. Djurado, D. Montinaro, J. Laurencin. Electrode Kinetics of Porous Ni-3YSZ Cermet Operated in Fuel Cell and Electrolysis Modes for Solid Oxide Cell Application. Electrochimica Acta, 389, 2021, 138765.

[2] F. Monaco, M. Hubert, J. Vulliet, J.P. Ouweltjes, D. Montinaro, P. Cloetens, P. Piccardo, F. Lefebvre-Joud, J. Laurencin. Degradation of Ni-YSZ Electrodes in Solid Oxide Cells: Impact of Polarization and Initial Microstructure on the Ni Evolution. Journal of The Electrochemical Society, 166 (15), 2019, F1229-F1242.

[3] A. Abaza, J. Laurencin, A. Nakajo, S. Meille, J. Debayle, D. Leguillon. Prediction of Crack Nucleation and Propagation in Porous Ceramics using the Phase-field Approach. Theoretical and Applied Fracture Mechanics, 119, 2022, 103349.

[4] A. Abaza, S. Meille, A. Nakajo, D. Leguillon, M. Hubert, C. Lenser, J. Laurencin. Fracture of Porous Ceramics: Application to the Mechanical Degradation of Solid Oxide Cell during Redox Cycling. ECS Transactions. 103, 2021, 1151.

[5] A. Abaza. Fracture of Porous Ceramics: Application to the Mechanical Degradation of Solid Oxide Cells during Redox Cycling. PhD thesis, Univ. Grenoble-Alpes, France.

[6] E. Effori, J. Laurencin, E. Da Rosa Silva, M. Hubert, T. David, M. Petitjean, G. Geneste, L. Dessemond, E. Siebert. An Elementary Kinetic Model for the LSCF and LSCF-CGO Electrodes of Solid Oxide Cells: Impact of Operating Conditions and Degradation on the Electrode Response. Journal of The Electrochemical Society, 168, 2021, 044520.

[7] C. Montella, V. Tezyk, E. Effori, J. Laurencin, E. Siebert. Linear Sweep and Cyclic Voltammetry of Porous Mixed Conducting Oxygen Electrode: Formal Study of Insertion, Diffusion and Chemical Reaction Model. Solid State Ionics, 359, 2021, 115485.

[8] E. Effori, J. Laurencin, V. Tezyk, C. Montella, L. Dessemond, E. Siebert. A Physically-based Modelling to Predict the Cyclic Voltammetry Response of LSCF-type Electrodes: Impact of the Ohmic Losses and Microstructure. Solid State Ionics, 371, 2021, 115765.

II. Multiscale models for cell performance and degradation rate prediction (UNIGE)

UNIGE task consisted in developing and validating an effective model for solid oxide cell performance and durability as a function of working and microstructure parameters, following physics-based principles. In view of the complexity of studied systems and the overlapping of different phenomena, a multiscale approach was applied. This allowed the choice of the most suitable tool depending on cell scale and desired level of analysis details, reducing at the same time the computation efforts to make it competitive with other available commercial software for cell simulation. SIMFC/SIMEC (SIMulation of Fuel Cells and Electrolysis Cells) can evaluate solid oxide cell operation in both fuel cell and electrolysis mode, starting from a 0D in home-built Fortran model executed in the process simulation software Aspen Plus to a higher-level in home-built Fortran model which analyses local phenomena on cell plane as well as interactions between stacked planar units [1]. Through the validation with experimental results, SIMFC/SIMEC was tuned at nominal state (i.e., at time equal to zero) by underlining the influence of working conditions on electrochemical performance in term of voltage and power which are the most descriptive cell outlets. Note the knowledge of the initial state-of-health is a fundamental step preliminary to any following study on degradation. Then specific degradation functions were implemented deriving them both empirically from electrochemical characterization data through a macroscale approach and by referring to specific microstructure changes through a microscale analysis. Here the result is a model able to estimate the Remaining Useful Life (RUL) in relation to a defined cell operation profile, also predicting the time evolution of main physicochemical features. Followed steps are schematised in Figure II.1 and they are discussed into details in subsequent sections.

Figure II.1 UNIGE activity performed steps from nominal cell characterization to RUL estimation through SIMFC/SIMEC.

Looking at the followed methodology, SIMFC/SIMEC is a physics-based model to predict cell performance solving conservation equations (i.e., material, charge, momentum and energy balances) on single cell or stack in case of a lumped parameter approach and in each specific sub-unit resulting from single cell plane discretization through a local level analysis. However, the key-point is the electrochemical kinetics which allows the simulation of both fuel cell and electrolysis operation just setting the current density direction without changing equations and parameters, differently from reference studies [2,3,4]. Following electrochemistry basic principles, the cell voltage derives from Nernst equilibrium value algebraically adding the polarization terms. The model considers a Fickian type diffusion as gas transport mechanism inside electrodes, a reaction rate according to Butler-Volmer equation and a thermal activated process for the ion and electron transfer. Main formulas are reported in Table II.1 (refer to authors' works if interested in kinetics complete description [5,6]). In such equations the degradation functions were introduced to evaluate the voltage variation along system operation. According to a macroscale approach, global cell degradation was computed by introducing further overpotential terms derived empirically from the time evolution of EIS spectra and characteristic curve slope. Whereas, focusing on different layers of the cell, more specific equations were considered to correlate the processes observed experimentally with microstructural and consequent kinetic parameter changes.

Table II.1 Kinetics formulation for solid oxide cell operation as both fuel cell and electrolyser.

Cell voltage	$V_{SOC} = E_{eq} \mp V_{\text{ohm}} \mp V_{act} \mp V_{diff}$
Equilibrium voltage	$E_{eq} = E^0(T) + \frac{RT}{zF} \ln\left(\frac{p_{H_2} p_{O_2}^{0.5}}{p_{H_2O}}\right)$
Ohmic overpotential	$V_{\text{ohm}} = \sum \frac{\delta}{\sigma} J = \gamma_{ohm} T \exp^{\left(\frac{E_{act,ohm}}{RT}\right)} J$
Activation overpotential	$V_{act} = \frac{2RT}{zF} \sinh^{-1}\left\lvert\frac{J}{2J_0}\right\rvert$ where $J_{0,fuel} = \gamma_{fuel} (y_{H_2})^A (y_{H_2O})^B \exp^{-\left(\frac{E_{act,fuel}}{RT}\right)}$ $J_{0,air} = \gamma_{air} (y_{O_2})^C \exp^{-\left(\frac{E_{act,air}}{RT}\right)}$
Diffusion overpotential	$V_{diff,fuel} = \frac{RT}{zF} \ln\left\{\frac{\left[1 \pm \frac{RTJ}{zFp_{H_2O}}\left(\frac{\delta_{sup}}{D_{H_2O\_sup}} + \frac{\delta_{act}}{3D_{H_2O\_act}}\right)\right]^{2B}}{\left[1 \mp \frac{RTJ}{zFp_{H_2}}\left(\frac{\delta_{sup}}{D_{H_2\_sup}} + \frac{\delta_{act}}{3D_{H_2\_act}}\right)\right]^{2A}}\right\}$ $V_{diff,air} = \frac{2RTC}{zF} \ln\left[\frac{p_{O_2}\theta_{O_2}}{p - (p - p_{O_2}\theta_{O_2}) \exp\left(\pm\frac{\theta_{O_2} RT \delta_{air} J}{zFpD_{O_2}}\right)}\right]$
List of symbols: *A*, *B*, *C* = Kinetic order, *D* = Diffusion coefficient, E^0 = Reversible voltage, E_{eq} = OCV voltage, E_{act} = Activation energy (*fuel* = H_2 electrode, *air* = O_2 electrode), *F* = Faraday constant, *J* = Current density, J_0 = Exchange current density, *p* = Pressure, *R* = Ideal gas constant, *T* = Temperature, *V* = Cell voltage-overpotential, *y* = Molar fraction, *z* = Number of transferred electrons, γ = Pre-exponential coefficient, δ = Electrode thickness (*act* = active layer, *sup* = support), θ = Diffusivity ratio coefficient.	

Followed sections illustrate the requested steps to build and tune SIMFC/SIMEC, discussing some of more indicative case studies developed during AD ASTRA project.

II.1 State-of-Health characterization

Before analysing possible degradation mechanisms, it was fundamental to tune the model on the reference performance of two commercial cells tested within AD ASTRA consortium, adapting the kinetics formulation to consider specific used material features and structures. Both Anode Supported Cell (ASC) consisting in Ni-YSZ/YSZ/LSCF-CGO and Electrolyte Supported Cell (ESC) consisting in Ni-CGO/YSZ/LSCF-CGO were studied thanks to DTU collaboration, which provided a detailed experimental dataset for fuel cell behaviour at variable temperatures, loads, fuel and oxidant compositions. Electrochemical characterization including EIS spectra and DRT analysis was performed to identify specific frequencies for each resistance and here to derive the main kinetic parameters requested into the model, such as activation energies and reactant kinetic orders. After reaching an average relative error lower than 1-2 % as model validation, 2D simulation by SIMFC/SIMEC allowed for underlining cell operation differences looking at global performance [7]

as well as current density and consequent overpotential spatial evolutions on the cell plane through a local level analysis [8]. As preliminary observations at 1073 K and variable feeds (Figure II.2), a lower slope of characteristic curves is visible in ASC which results to be about a third of ESC case in view of its thicker electrolyte used as a support (i.e., higher internal resistance). ESC profiles are quite linear suggesting the main weight of the ohmic overpotential, whereas in ASC a different trend is underlined above all at low current densities where the quite rapid voltage decrease highlights also effects of activation term.

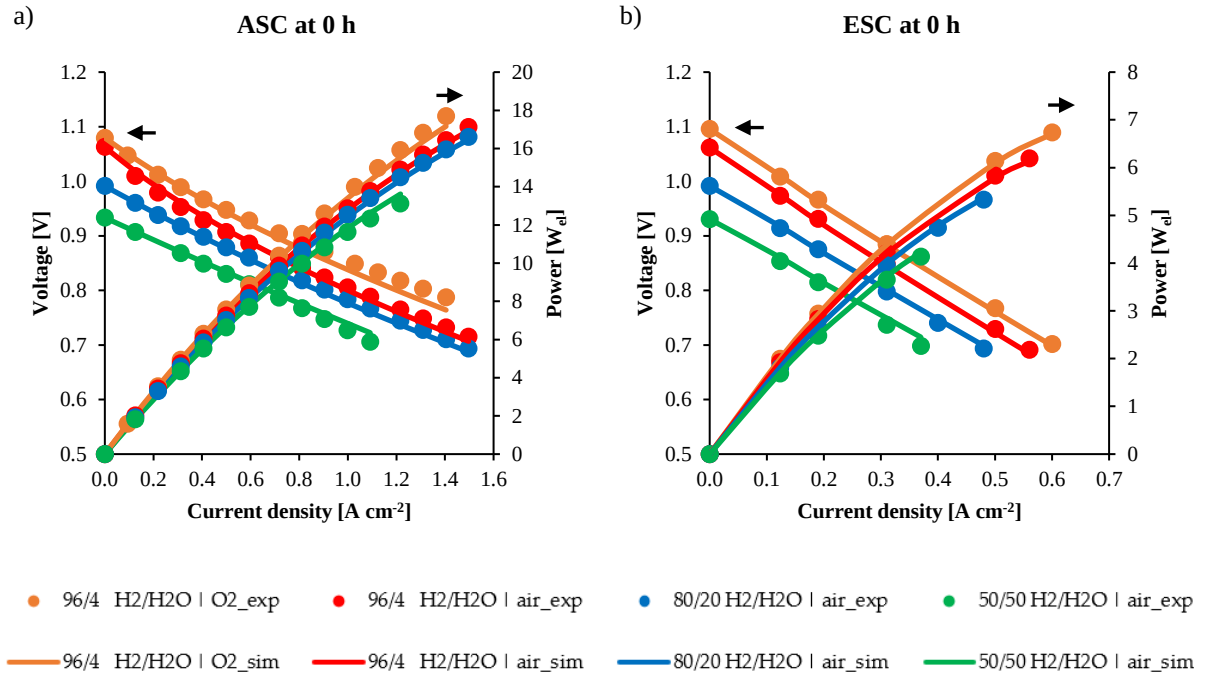

Figure II.2 ASC (a) vs. ESC (b) characteristic curves at 1073 K at variable reactant volumetric compositions according to experimental and SIMFC/SIMEC results.

Different cell contributions were evaluated dividing the total overpotential into ohmic, activation and diffusion term as a function of the working point. As expected the ohmic overpotential has the main role in the ESC configuration with a weight >80 %. Whereas the activation polarization is more significant in ASC case, where it can reach also the ~60 % under a dry anodic feed (4 %vol of steam). In view of specific fuel electrode materials, Ni-CGO anode shows a lower activation overpotentials since the reaction occurs also at double phase boundary sites [9]. On the contrary, in the Ni-YSZ configuration the electrochemical reaction is limited to the triple phase boundary points into the functional layer. In both configurations steam content favours the kinetics reducing the activation overpotential, since it favours Ni-YSZ surface processes [10] and has an autocatalytic effect accelerating hydrogen oxidation in Ni-CGO [11]. Looking at oxidant influence, a pure oxygen inlet stream causes a reduction of only one percentage point compared to air case in both designs confirming a lower dependence. Since all chosen working conditions avoid high fuel utilizations, the weight of diffusion overpotential is always minimum, above all in ESC due to the thin anode. Focusing now on a specific working point to evaluate local performance, it was assumed an electric load of 0.3 A cm^{-2} and a feed composition of 80/20 %vol H_2/H_2O for the fuel and dry air at 1073 K which results in a voltage of 0.931 V and 0.818 V in case of ASC and ESC respectively. For instance, Figure II.3 shows maps of ESC ohmic and ASC fuel activation overpotentials representing the main losses for each of these designs respectively. Working under co-flow fuel feeding, electrochemical processes go forward along the flow direction resulting in higher detected resistances at the inlet, where the reaction is faster, in both maps. A significant gradient between inlet and outlet area is highlighted, above all considering ASC anodic activation overpotentials due to the increasing water

content along the flow direction which reduces the polarization losses. ESC ohmic contribution is characterised by a minor gradient assuming an isothermal behaviour in view of small cell scale (4x4 cm^2).

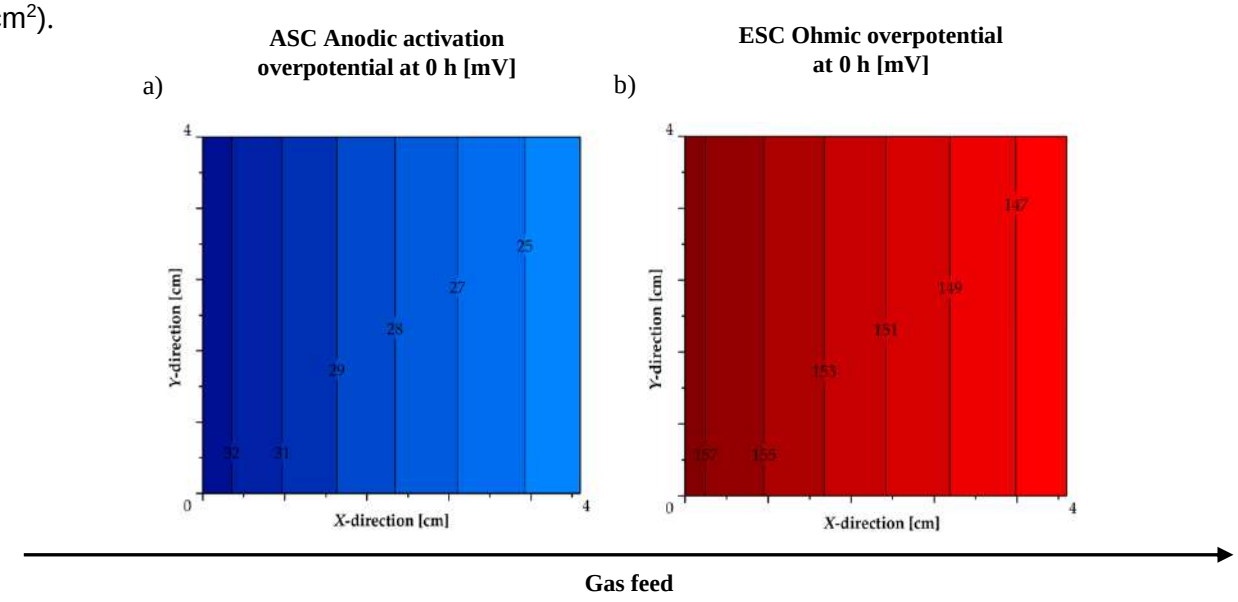

Figure II.3 Fuel cell local performance feeding 80/20 %vol H_2/H_2O mixture and dry air at 1073 K and 0.3 A cm^{-2} in terms of ASC activation overpotential at fuel electrode (a) and ESC ohmic overpotential of global cell (b).

II.2 Degradation function introduction

A multiscale approach was followed to identify the degradation functions depending on the available information. At macroscale, empirical equations were derived by analysing EIS spectra and characteristic curves measured at different times during cell testing, which were introduced as further time dependent overpotential terms distinguishing between the increase of ohmic and polarization (i.e., activation and diffusion) contributions (Equation II.1). The first was evaluated knowing the time profile of internal resistance from EIS spectra, whereas the second considered the punctual variation of the differential resistance for available characteristic curves. Here, the degradation loss formulations, V_{deg}, were detected as a function of current density J and time t.

$$V_{SOC} = E_{eq} \mp V_{ohm} \mp V_{act} \mp V_{diff} \mp V_{deg,ohm}(t,J) \mp V_{deg,pol}(t,J) \quad \text{(II.1)}$$

When a more detailed characterisation was performed, degradation functions were directly introduced in formulated overpotential terms (Table II.1), expressing different kinetic parameters dependent on time. In view of the significant correlations between polarization losses and the operation point, more complex experimental tests had to be performed to evaluate the kinetics evolution as a function of both time and working conditions, so also requiring ex-situ tests on specific components of the cell. For instance, looking at cathodic coated interconnect, some empirical correlations were detected for the pre-exponential coefficient γ_{ohm} and the activation energy, $E_{act,ohm}$, of its ohmic overpotential (Equation II.2). These were obtained both monitoring the area specific resistance during durability tests of interconnect samples as well as through cooling ramps at different ageing times in view of the significant thermal dependence [12].

$$V_{ohm}(t) = \gamma_{ohm}(t)\exp\left[\frac{E_{act,ohm}(t)}{RT}\right]J \quad \text{(II.2)}$$

Finally, at lower-level analysis the microstructural changes were correlated to kinetic parameters to simulate the specific degradation of each layer. In view of the significant weight of Ni-based electrode degradation on global cell performance, the percolation theory was introduced into SIMFC/SIMEC

kinetics to express overpotential parameters as a function of particle radius and phase fraction (Table II.2). The Ni-cermet layer is modelled as a binary system with a random packaging of spheres corresponding to metal and ceramic particles combined to form the percolated cluster. Electrode ohmic resistance depends on thickness and conductivity calculated as the sum of Ni and ceramic contributions knowing the conductivity of the dense solid material, σ_0, and the threshold solid phase fraction, Ψ^t. Whereas the exchange current density, J_0, in the activation overpotential depends on Triple Phase Boundary (TPB) length, $l_{\mathrm{TPB}}^{\mathrm{eff}}$, computed considering the available exchange area among phases as well as the probability to belong a percolated cluster.

Table II.2 Percolation theory formulation into SIMFC/SIMEC electrochemical kinetics to consider Ni-YSZ electrode dependences on microstructural parameters.

Kinetics term	Physicochemical feature
For ohmic overpotential $V_{ohm,fuel} = \frac{\delta_{fuel}}{\sigma_{Ni}^{eff} + \sigma_{YSZ}^{eff}} J$	$\sigma_i^{eff} = \sigma_{i,0}(1-\varepsilon)^2 \left[\frac{\Psi_i - \Psi_i^t}{1-\Psi_i^t(1-\varepsilon)}\right]^2$ $\Psi_i^t = \frac{1.764 r_i}{(\overline{Z^\dagger} - 1.764) r_j + 1.764 r_i}$ $\sigma_{Ni,0}[Sm^{-1}] = 3.27 \times 10^6 - 1065.3T[K]$ $\sigma_{YSZ,0}[Sm^{-1}] = 6.24 \times 10^4 \exp^{-\left(\frac{10{,}300}{T[K]}\right)}$
For activation overpotential $J_{0,fuel} = \gamma'_{fuel} l_{TPB}^{eff} y_{H_2}^A y_{H_2O}^B exp^{-\left(\frac{E_{act,fuel}}{RT}\right)}$	$l_{TPB}^{eff} = \frac{3(1-\varepsilon)\Psi_{Ni}}{4r_{Ni}^3}\left[\sin\left(\frac{\pi}{12}\right)\min(r_{Ni}, r_{YSZ})\right]\frac{\left(1+\frac{r_{Ni}^2}{r_{YSZ}^2}\right)\Psi_{YSZ} r_{Ni} \overline{Z^\dagger}}{\Psi_{YSZ} r_{Ni} + \Psi_{Ni} r_{YSZ}} p_{Ni} p_{YSZ}$ $p_i = \left[1 - \left(\frac{4.236 - Z^\dagger{}_{i,i}}{2.472}\right)^{2.5}\right]^{0.4}$

List of symbols: A, B = Kinetic order, E_{act} = Activation energy, J = Current density, J_0 = Exchange current density, l_{TPB} = TPB length, p = Percolated network probability, R = Ideal gas constant, r = Radius, T = Temperature, V = Overpotential, y = Molar fraction, γ' = Pre-exponential coefficient, $Z^\dagger$= Coordination number, δ = Electrode thickness, ε = Porosity, σ = Conductivity, Ψ = Solid phase fraction, Ψ^t = Threshold solid phase fraction.

II.3 Degradation rate evolution

According to introduced degradation functions, devoted case-studies are here discussed to underline SIMFC/SIMEC prospective uses. All requested experimental data for model tunning were shared within AD ASTRA consortium. Note different information can be deduced depending on the level of analysis. At macroscale, empirical correlations allow the simulation of voltage time variation after relatively few experimental measurements, but only preliminary assumptions on occurring degradation mechanisms can be supposed. On the other hand, the local level analysis correlates voltage losses to specific degradation sources by evaluating kinetic parameter dependences on microstructure. Nevertheless, in this second case the performance simulation is more difficult

requiring many experimental data on material structure changes. Here, pictures of cell behaviour at cadenced instances are more feasible, instead of the working time complete profile.
As the durability index, the percentage Degradation Rate, $DR_{\%}$, is commonly used representing how the cell voltage varies during the time. It is calculated as the absolute difference between the voltage at generic time, V_t, and its initial value (at the test start or at the beginning of considered interval), V_0, normalized with respect to V_0 and over the time step duration, t. It is typically expressed as percent change per 1000 hours (Equation II.3).

$$DR_{\%} = \left|\frac{V_t - V_0}{V_0}\right| \frac{1000}{t} \; 100\ \% \tag{II.3}$$

The validation of macroscale approach was performed on data referred to a small-scale anode supported fuel cell consisting in Ni/YSZ/YSZ/LSCG-CGO, which worked in galvanostatic mode for more than 9000 hours feeding dry hydrogen and ait at 1023 K [13]. A good match was obtained by comparing simulated and experimental values for voltage evolution as well as characteristic curves (relative error lower than 2 %), as shown in Figure II.4. In this test $DR_{\%}$ is equal to -0.8 V% kh^{-1} characterised by a faster reduction in the first 2000 h ($DR_{\%}$ equal to -1.2 V% kh^{-1}) and a followed lower one ($DR_{\%}$ equal to -0.5 V% kh^{-1}). The degradation is mainly due to the increase of ohmic loss which changes of ~50 mV (46 % increase) at the reference working condition of 0.5 A cm^{-2}.

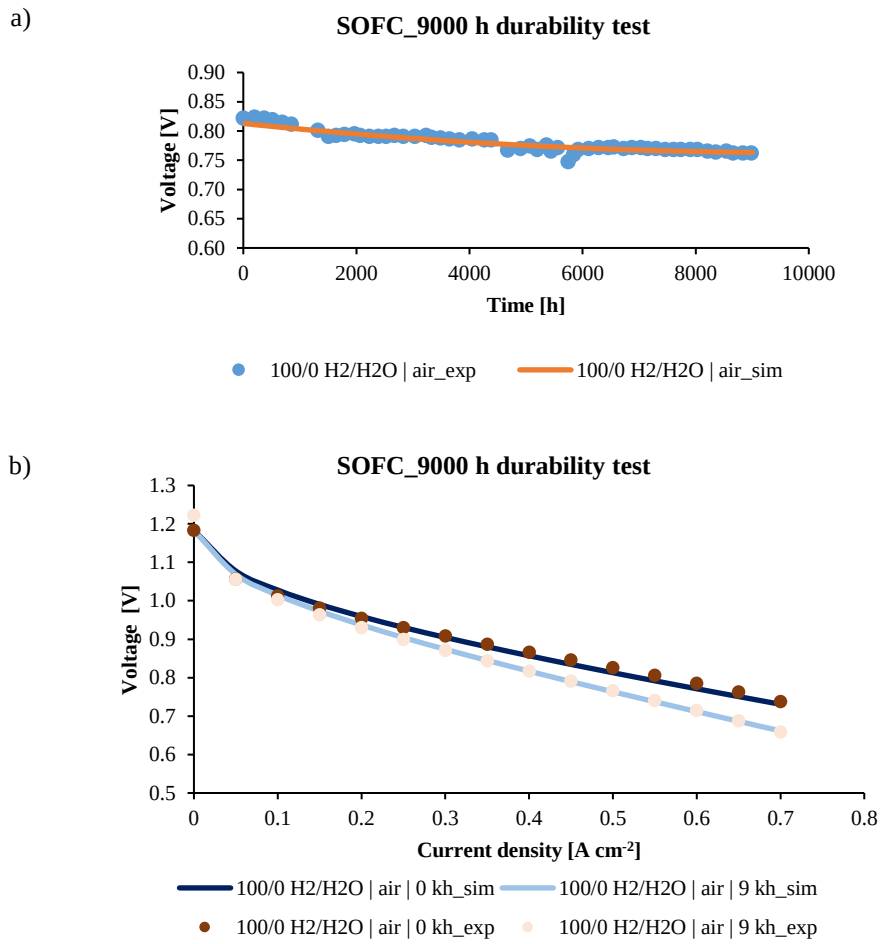

Figure II.4 Model validation looking at durability tests under 0.5 A cm^{-2} (a) and characteristic curves at different operation hours (b) feeding dry hydrogen and air at 1023 K.

If the previous approach is useful for cell control under operation requiring just electrochemical characterization measurements for model tunning, the study of each layer degradation is not easy

in full cell performance analysis in view of possible concurrent effects. Here, the model was used to evaluate the weight of a specific degradation process on global system behaviour basing on ex-situ tests of single layers. As example, referring to previously shown equation on aged cathodic coated interconnects (Equation II.2), the influence of CuMnO/AISI441 on a commercial scale anode supported fuel cell was studied under co-flow feeding adiabatic conditions [12]. Initial state-of-health characterization as discussed in Section II.1 was used to predict cell reference performance [8], whereas the degradation function for coated interconnect derived from ex-situ tests carried out by DCCI-UNIGE. Imposing a galvanostatic operation for 400 hours and 1023 K as the inlet temperature, the correspondent $DR_{\%}$ values were computed for different loads between 40 h and 400 h when the best and the worst voltage values were detected in view of the sample initial contact improvement. In agreement with ohmic law (Table II.2), the resistance worsens at current density increase (Figure II.5-a). Anodic feed also shows a significant influence, despite the interconnect ohmic resistance does not depend on gas composition. The $DR_{\%}$ is around 8 time higher using a biogas as fuel instead of a wet hydrogen mixture due to different cell thermal behaviour. Indeed, under direct internal reforming operation there is a significant temperature drop at the inlet (Figure II.5-b) due to endothermic steam reforming reaction which causes a significant increase of ohmic overpotential (Figure II.5-c) because of a higher activation energy of aged interconnects.

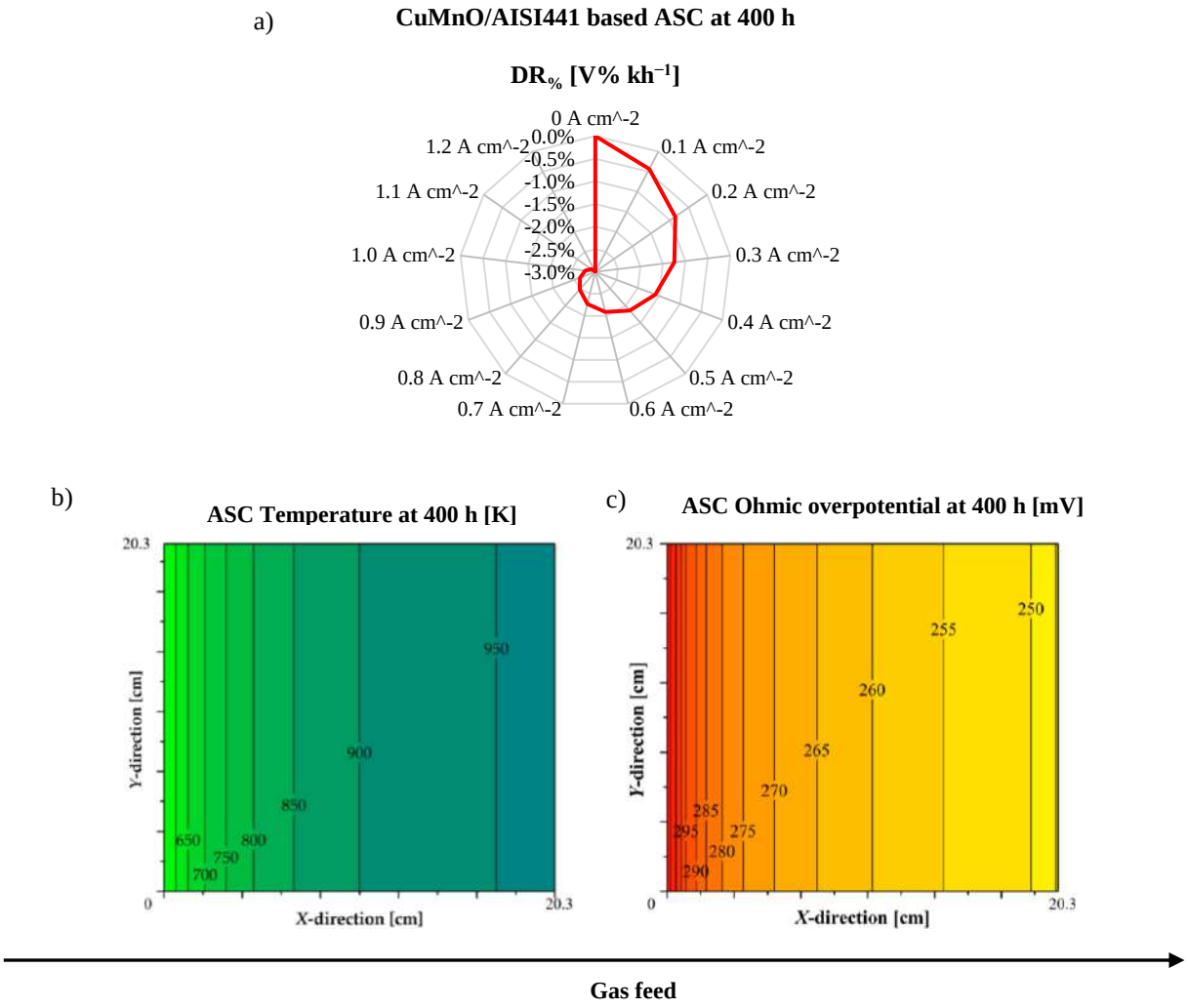

Figure II.5 $DR_{\%}$ under different loads at 1023 K inlet temperature and feeding a wet hydrogen mixture and air as oxidant (a), local maps of temperature (b) and ohmic overpotential (c) after 400 h under direct internal reforming operation at 0.4 A cm^{-2}.

Finally, as an example of microscale level simulation, the performance of aged hydrogen electrode based on Ni-YSZ in ASC and Ni-CGO in ESC was simulated after 1000 h operation in fuel cell mode co-flow feeding an anodic wet hydrogen mixture and air as oxidant [14]. Indeed, the hydrogen electrode is one of the most critical elements in a cell. Referring to Ni-YSZ based ASC tested at 0.4 A cm^{-2} and 1023 K, microstructural analysis performed by DTU underlines main changes above all in the functional layer (i.e., the zone near to electrolyte interface), where Ni agglomeration is detected showing a particle size increase of ~40 % as compared to the reference sample with a bit higher values in the outlet section. Ni fraction also decreases of ~50 % points in aged cell, resulting in porosity increase. Looking at electrochemical kinetics, these processes influence above all the catalytic activity dependent on exchange current density and here TPB length (Table II.2). Indeed, it decreases after 1000 h working with lower values at the aged sample outlet, suggesting the produced steam as accelerating degradation factor in view of its higher content (Figure II.6-a), as already reported in previous literature [15,16]. Considering this trend, the anodic activation overpotential of aged cell becomes 2.5 times higher than nominal case, showing a minimum profile along the flow direction (Figure II.6-b) differently from reference cell map (Figure II.3-a). Indeed, higher values characterize (i) the inlet since the reaction develops above all in the first centimeters of cell plane resulting in higher local current density as observed in nominal case, and (ii) the outlet where larger Ni radii are detected worsening the electrode performance.

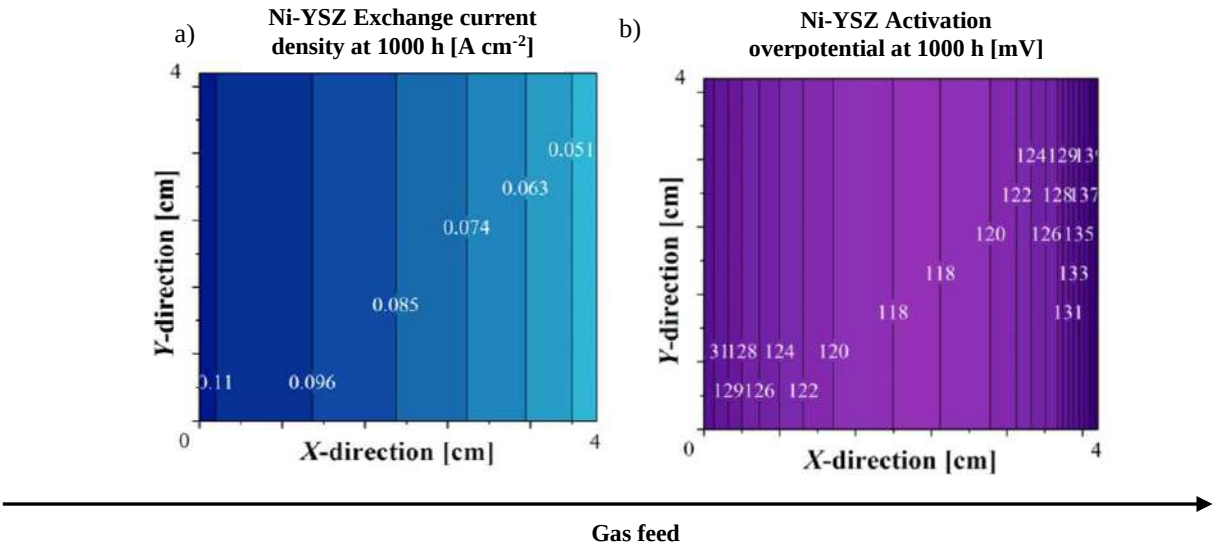

Figure II.6 Ni-YSZ electrode properties considering OCV exchange current density (a) and resulting anodic activation overpotential under 0.4 A cm^{-2} (b) after 1000 h operation at 1023 K and feeding 96/4 %vol H_2/H_2O mixture and dry air.

Considering the ageing of Ni-CGO based ESC after 1000 h operation at 0.2 A cm^{-2} and 1123 K, the main variations characterize the ohmic overpotential partially due to hydrogen electrode degradation. Differently from the quite homogenous Ni-YSZ initial composition, ESC electrode is composed by three sections: a pure CGO layer at electrolyte interface, the effective catalytic zone of Ni-CGO cermet and a Ni top layer to improve conductivity. After ageing, the microstructural features of CGO barrier layer are almost unchanged with comparison to the reference cell, but its thickness is increased due to Ni migration away from the zone adjacent to the electrolyte. At the top contact layer, the percolating Ni rises at both inlet and outlet to ~60 %, and a significant Ni particle coarsening is also detected resulting in ~30 % size increase compared to the initial structure. Such phenomena cause Ni-CGO total ohmic resistance averaged increase of ~50 %, due to above all Ni loss near to the interface with electrolyte (Figure II.7). Ni coarsening and above all porosity increase also cause the reduction of Ni contact layer conductivity. However, the computed variations are quite negligible

with respect to global cell measured ohmic resistance which is mainly influenced by ionic conductor layers (i.e., YSZ electrolyte and CGO barrier layer).

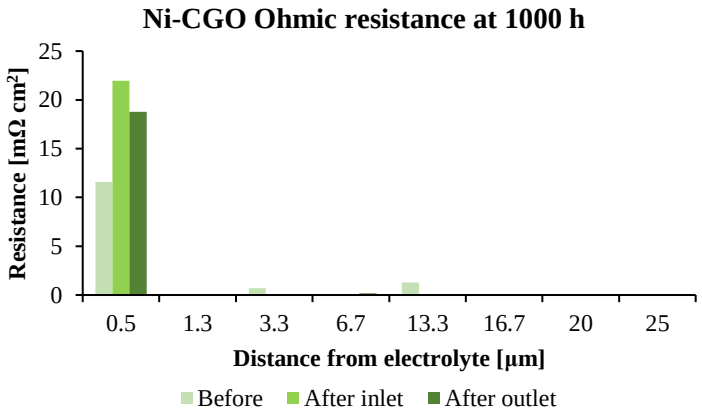

Figure II.7 Ohmic resistance along Ni-CGO electrode thickness for nominal state, at inlet and outlet sections after 1000 h operation at 1123 K and 0.2 A cm^{-2} feeding 96/4 %vol H_2/H_2O mixture and dry air.

REFERENCES

[1] F.R. Bianchi, A. Baldinelli, L. Barelli, G. Cinti, E. Audasso, B. Bosio. Multiscale Modeling for Reversible Solid Oxide Cell Operation. Energies, 13(19), 2020, 5058.
[2] F. Lonis, V. Tola, G. Cau. Renewable Methanol Production and Use through Reversible Solid Oxide Cells and Recycled CO_2 Hydrogenation. Fuel, 246, 2019, 500–515.
[3] M. Ni, M. Leung, D. Leung. Parametric Study of Solid Oxide Steam Electrolyzer for Hydrogen Production. International Journal of Hydrogen Energy, 32(13), 2007, 2305–2313.
[4] M. Hauck, S. Herrmann, H. Spliethoff. Simulation of a reversible SOFC with Aspen Plus. International Journal of Hydrogen Energy, 42(15), 2017, 10329–10340.
[5] F.R. Bianchi, B. Bosio, A. Baldinelli, L. Barelli. Optimization of a Reference Kinetic Model for Solid Oxide Fuel Cells. Catalysts, 10(1), 2020, 104.
[6] F.R. Bianchi, R. Spotorno, P. Piccardo, B. Bosio. Solid Oxide Fuel Cell Performance Analysis through Local Modelling. Catalysts, 10(5), 2020, 519.
[7] A.K. Padinjarethil, F.R. Bianchi, B. Bosio, A. Hagen. Anode and Electrolyte Supported Solid Oxide Fuel Cells: Experimentation and Modelling. European Fuel Cell Forum, October 2020.
[8] A.K. Padinjarethil, F.R. Bianchi, B. Bosio, A. Hagen. Electrochemical Characterization and Modelling of Anode and Electrolyte Supported Solid Oxide Fuel Cells. Frontiers in Energy Research, 9, 2021, 668964.
[9] M. Riegraf, V. Yurkiv, R. Costa, G. Schiller, K. A. Friedrich. Evaluation of the Effect of Sulfur on the Performance of Nickel/Gadolinium-Doped Ceria Based Solid Oxide Fuel Cell Anodes. ChemSusChem, 10(3), 2017, 587–599.
[10] W.G. Bessler, M. Vogler, H. Störmer, D. Gerthsen, A. Utz, A. Weber, E. Ivers-Tiffée. Model Anodes and Anode Models for Understanding the Mechanism of Hydrogen Oxidation in Solid Oxide Fuel Cells. Physical Chemistry Chemical Physics, 12(42), 2010, 13888.
[11] M. Athanasiou, D.K. Niakolas, S. Bebelis, S. G. Neophytides. Steam effect on Gerischer Impedance Response of a Ni/GDC|YSZ|LSM Fuel Cell/anode. Journal of Power Sources, 448, 2020, 227404.
[12] R. Spotorno, F.R. Bianchi, D. Paravidino, B. Bosio, P. Piccardo. Test and Modelling of Solid Oxide Fuel Cell Durability: A Focus on Interconnect Role on Global Degradation. Energies, 15(8), 2022, 2762.
[13] Z. Stoynov, D. Vladikova, B. Burdin, J. Laurencin, D. Montinaro, G. Raikova, G. Shiller, P. Szabo. Differential Analysis of SOFC Current-Voltage Characteristics. Applied Energy, 228, 2018, 1584–1590.
[14] A.K. Padinjarethil, F.B. Bianchi, B. Bosio, A. Hagen. Degradation of Ni-YSZ and Ni-GDC Fuel cells After 1000 h Operation: Analysis of Different Overpotential Contributions According to Electrochemical and Microstructural Characterization. European Fuel Cell Conference, December 2021, Online Conference.
[15] L. Holzer, B. Iwanschitz, Th. Hocker, B. Münch, M. Prestat, D. Wiedenmann, U. Vogt, P. Holtappels, J. Sfeir, A. Mai, T. Graule. Microstructure Degradation of Cermet Anodes for Solid Oxide Fuel Cells: Quantification of Nickel Grain Growth in Dry and in Humid Atmospheres. Journal of Power Sources, 196(3), 2011, 1279–1294.
[16] M.B. Mogensen, M. Chen, H. L. Frandsen, C. Graves, A. Haunch, P. Van Hendriksen, T. Jacobsen, S.H. Jensen, T.L. Skafte, X. Sun. Ni Migration in Solid Oxide Cell Electrodes: Review and Revised Hypothesis. Fuel Cells, 2021, fuce.202100072.

III. Dynamic lumped parameter models for degradation accelerating factor identification (UNISA)

The lumped parameter model designed by UNISA is meant to simulate SOC operation in both fuel cell and electrolyser modes. To do so, key electrochemical equations and cell microstructure parameters are introduced and improved starting from the model already proposed in the work of Polverino et al. [1]. In such way, the degradation phenomena detailed within the project can be mathematically simplified and embedded in this model to have a comprehensive but fast simulation platform for degradation rate estimation and the identification of accelerating factors.

III.1 SOC lumped model description

To design the model according to samples and data coming from the AD ASTRA project, the electrode supported SOC already accounted by CEA (and fully addressed in their works) is here considered. The single cell layers are the following [2,3,4]: (i) Ni-YSZ hydrogen electrode (with cell support function), (ii) dense YSZ electrolyte, (iii) CGO barrier layer, (iv) oxygen electrode with multi-layer structure (a MIEC made of LSCF+CGO directly in contact with the barrier layer and a single substrate of LSCF, located between the MIEC and the current collector), and (v) LSC current collector. The key structural features considered in the model are listed in Table III.1.

Table III.1 Structural features of the CEA reference SOC requested for UNISA lumped parameter model.

Parameter	H_2 electrode	Electrolyte	Barrier layer	O_2 electrode bottom	O_2 electrode top	Current collector
Composition	Ni+YSZ	dense YSZ	CGO	LSCF+CGO	LSCF	LSC
Thickness [µm]	260	8	5	15	18	20
Porosity [-]	0.29	-	-	0.435	0.513	-
Ni vol. frac [-].	0.287	-	-	-	-	-
YSZ vol. frac. [-]	0.423	-	-	-	-	-
LSCF vol. frac. [-]	-	-	-	0.301	0.487	-
CGO vol. frac. [-]	-	-	-	0.264	-	-
Ni diam. [µm]	0.46	-	-	-	-	-
YSZ diam. [µm]	0.37	-	-	-	-	-
LSCF diam. [µm]	-	-	-	0.38	-	-
CGO diam. [µm]	-	-	-	0.32	-	-
Tortuosity [-]	1.67	-	-	1.55	1.66	-

The single cell voltage V_{sc} is modelled by subtracting to the Nernst potential V_{ner} the different polarization losses (Equation III.1).

$$V_{sc}=V_{ner}-V_{act}-V_{ohm}-V_{con}-V_{off} \quad \text{(III.1)}$$

Where V_{act}, V_{ohm}, V_{con} and V_{off} are the activation, ohmic, concentration and offset losses, respectively. The Nernst voltage is modelled as in Equation III.2.

$$V_{ner} = 1.274 - 2.765 \cdot 10^{-4} T[K] + \frac{RT}{2F} \ln\left(\frac{p_{H_2} p_{O_2}^{0.5}}{p_{H_2O}}\right) \quad \text{(III.2)}$$

The activation losses are modelled through an adapted Tafel equation that applies for losses at both anode and cathode sides referring to fuel cell mode (Equations III.3, III.4 and III.5).

$$V_{act}=V_{act,an}+V_{act,ca} \quad \text{(III.3)}$$

$$V_{act,an} = \frac{J}{|J|} \frac{RT}{2\alpha F} \ln\left(1+\frac{|J|}{J_{ex,an}}\right) \quad \text{(III.4)}$$

$$V_{act,ca} = \frac{J}{|J|}\frac{RT}{2\alpha F}\ln\left(1+\frac{|J|}{J_{ex,ca}}\right) \quad \text{(III.5)}$$

Where the absolute value of the current density J is introduced to account for both fuel cell (positive current) and electrolysis (negative current) operation. $J_{ex,an}$ and $J_{ex,ca}$ are the exchange current densities at hydrogen and oxygen electrodes, respectively. These are proportional to the TPB lengths of each electrode through lumped coefficients k_{an} and k_{ca}, as shown in Equations III.6 and III.7.

$$J_{ex,an} = k_{an} l_{TPB,an}\left(\frac{p_{H_2}}{p_{ref}}\right)^{0.5}\left(\frac{p_{H_2O}}{p_{ref}}\right)^{0.5}\exp\left(-\frac{E_{act,an}}{RT}\right) \quad \text{(III.6)}$$

$$J_{ex,ca} = k_{ca} l_{TPB,ca}\left(\frac{p_{O_2}}{p_{ref}}\right)^{0.25}\exp\left(-\frac{E_{act,ca}}{RT}\right) \quad \text{(III.7)}$$

The ohmic loss is evaluated as the sum of each layer conduction resistance, being the ratio between layer thickness μ and conductivity σ (Equation III.8).

$$V_{ohm} = \sum \frac{\mu}{\sigma} J \quad \text{(III.8)}$$

Layer conductivities depend on the type of microstructure: in case of single material the conductivity is that of the dense solid, whereas, in case of multiple materials, percolation theory is accounted [1]. The dense solid material conductivities, expressed in S m^{-1}, are taken from the literature [1,4,5,6], as shown in Equations III.9, III.10, III.11, III.12 and III.13 for different cases.

$$\sigma_{Ni} = 3.27 \cdot 10^6 - 1065.3T \quad \text{(III.9)}$$

$$\sigma_{YSZ} = 6.25 \cdot 10^4 \exp\left(-\frac{10300}{T}\right) \quad \text{(III.10)}$$

$$\sigma_{CGO} = \frac{8.56 \cdot 10^6}{T}\exp\left(-\frac{65 \cdot 10^3}{RT}\right) - 1065.3T \quad \text{(III.11)}$$

$$\sigma_{LSCF} = 37177\left(p_{O_2}\right)^{\left(-0.52 p_{O_2}^{0.0275} + 0.558\right)} \quad \text{(III.12)}$$

$$\sigma_{LSC} = \frac{2.01 \cdot 10^8}{T}\exp\left(-\frac{3860}{RT}\right) \quad \text{(III.13)}$$

The concentration losses are as well expressed with respect to each electrode contribution, referring again to fuel cell mode into formulation (Equations III.14, III.15 and III.16).

$$V_{con} = V_{con,an} + V_{con,ca} \quad \text{(III.14)}$$

$$V_{con,an} = \frac{RT}{2F}\ln\left(1+\frac{J}{J_{lim,H_2O}}\right) - \frac{RT}{2F}\ln\left(1-\frac{J}{J_{lim,H_2}}\right) \quad \text{(III.15)}$$

$$V_{con,ca} = \frac{RT}{4F}\ln\left(1-\frac{J}{J_{lim,O_2}}\right) \quad \text{(III.16)}$$

Where the limiting current densities related to the reactants and products at both electrodes are formulated in Equations III.17, III.18 and III.19.

$$J_{lim,H_2O} = \frac{2FD_{an}^{eff} p_{H_2O}}{RT\mu_{an}} \quad \text{(III.17)}$$

$$J_{lim,H_2} = \frac{2FD_{an}^{eff} p_{H_2}}{RT\mu_{an}} \quad \text{(III.18)}$$

$$J_{lim,O_2} = \frac{4FD_{ca}^{eff} p_{O_2}}{RT\mu_{ca}} \quad \text{(III.19)}$$

The electrode diffusion coefficients take into account binary and Knudsen diffusion.
The initial version of the model published in [1] has already been verified on experimental data in fuel cell mode. The updated version presented in this deliverable has also been applied to the experimental data in electrolyser mode from CEA and published in the work of Monaco et al. [3]. The results are shown in Figure III.1, proving the good accuracy of the model and its capability to be applied in both fuel cell and electrolyser modes.

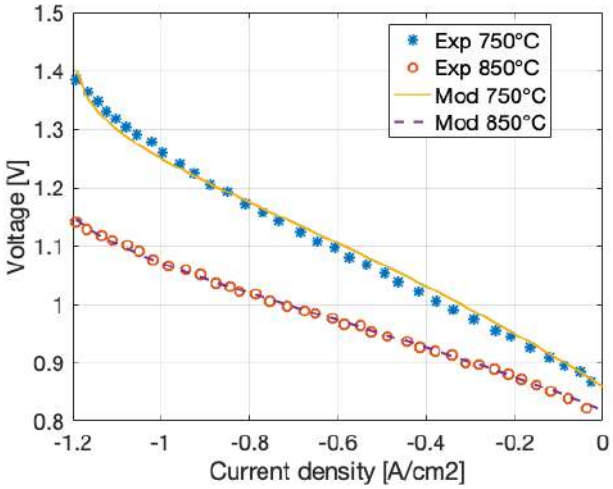

Figure III.1 UNISA lumped parameter model simulation of SOC operation in electrolyser mode and comparison with CEA experimental data from Monaco et al. [3].

To perform degradation rate estimation and accelerating stress factor identification, simplified degradation functions related to the mechanisms investigated in the project are introduced in the SOC performance model. In the following section, the Ni agglomeration mechanism addressed and modelled in detail by CEA is considered and discussed.

III.2 Implementation of low-level degradation model: Ni agglomeration example

The definition of a Ni agglomeration simplified model is essential for its implementation within the lumped performance model for degradation rate estimation according to the given operating conditions. A first study has been already conducted in [1], where the Ni agglomeration model was taken from literature, and it was properly used to identify the key accelerating stress factors for transfer function design.
To address data and models developed within the AD ASTRA project, the work done by CEA on the Ni agglomeration/coarsening (see Section I.1) is accounted for the simulation of Ni particle growth over time. The simplified model that expresses such behaviour depends on the initial Ni particle size and time according to Equations III.20 and III.21.

$$D_{Ni}(t) = \left[k_{pow} \cdot t + \left(D_{Ni}(t=0)\right)^n\right]^{1/n} \quad \text{(III.20)}$$

$$k_{pow} = k_0 \cdot \exp^{\left(-\frac{E_{act}}{RT}\right)} \quad \text{(III.21)}$$

The model has been checked with respect to the experimental observations performed by CEA and published in [3], as shown in Figure III.2.

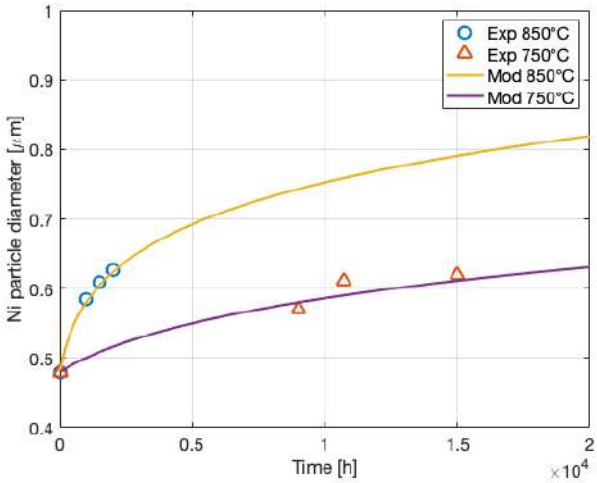

Figure III.2 Comparison of simplified Ni agglomeration model with experimental data from Monaco et al. [3] (conceived from CEA activity – Section I.1).

To further correlate the main affected mesoscale parameters to the Ni agglomeration model expressed with respect to Ni particle diameter, the link between the density of TPB length and Ni diameter growing over time is explicitly established as in Equation III.22.

$$l_{TPB,an}(t) = l_{TPB,an}(t=0)\frac{D_{Ni}(t=0)}{D_{Ni}(t)} \tag{III.22}$$

Through Equation III.22, the density of TPB length at the hydrogen electrode (that appears in Equation III.6) has an inverse correlation with the Ni particle diameter: indeed, it reduces over time since the diameter increases due to the agglomeration process. This reflects the loss in TPB that is one of the main effects of the degradation mechanism (as already remarked in [1]).
To check whether the simplified formulation is correct, the model is again compared with the experimental data of CEA (Section I.1) published in [3], and the results are shown in Figure III.3. From the achieved trends, the comparison can be considered satisfactory and useful for the purposes of singling out accelerating stress factors and building mathematical transfer functions.

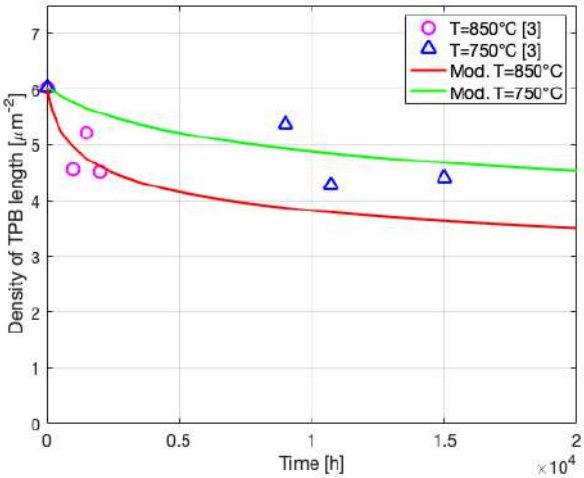

Figure III.3 Comparison of simplified degradation model for the density of TPB length subject to Ni agglomeration with experimental data from Monaco et al. [3] (conceived from CEA activity – Section I.1).

III.3 Transfer function generation method

The methodology to design mathematical transfer functions capable of correlating degradation rates and applied operating conditions has been fully presented and discussed in [1]. The proposed procedure has been structured in eight main steps, that are:

- Step 1: the identification of degradation mechanisms and the design of microscale parameter models;
- Step 2: the identification of the affected mesoscale parameters and the design of related models;
- Step 3: the design of an overall simplified performance model;
- Step 4: the link among the models through a multiscale approach;
- Step 5: the application of a parametric analysis to assess the influence of the operating conditions on degradation rate;
- Step 6: the identification of the accelerating stress factors;
- Step 7: the design of mathematical transfer functions to correlate accelerating factors and degradation rate;
- Step 8: the development of guidelines for lifetime estimation and AST protocol design.

In the work [1] such method has been applied to Ni agglomeration mechanisms, providing a mathematical transfer function with the following expression for the degradation rate ξ (Equation III.23).

$$\xi[mV/kh] = a_1 \exp^{a_2 T[°C]} (\exp^{a_4 J_N} - \exp^{a_4 J_N}) \quad \text{(III.23)}$$

The coefficients a_1, a_2, a_3 and a_4 are function of the hydrogen electrode pressure, whereas the explicit variables are the temperature T and the normalized current J_N density expressed as the ratio between the applied current density and the maximum one related to the specific working temperature and pressure. This function has been obtained through a first parametric analysis, which singled out the current density, the temperature and the hydrogen electrode pressure as accelerating stress factors. Then, the lumped performance model, with embedded low-level degradation functions, has been used to simulate degradation rates at different stress factor values, and the achieved results have been fitted to identify the coefficients necessary for the transfer function in Equation III.23.

The use of the proposed transfer function has been summarized through a surface map (Figure III.4), in which the degradation rate ξ is shown as a function of the temperature (x-axis) and normalized current density (y-axis) while keeping constant the hydrogen electrode pressure.

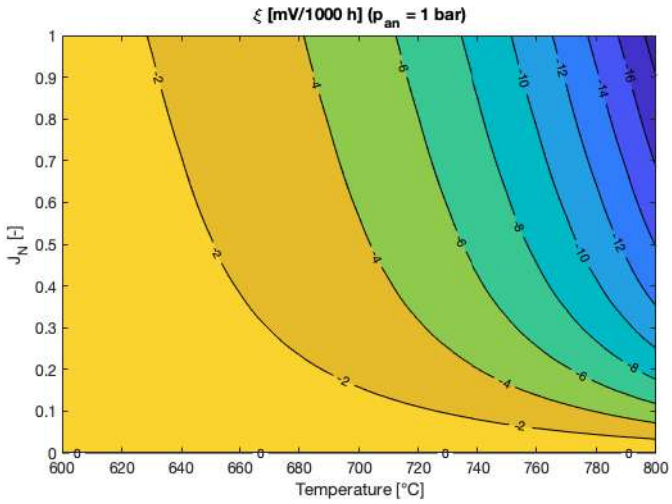

Figure III.4 Degradation rate map obtained through the mathematical transfer function shown in Equation III.23, with variable temperature and normalized current density and given hydrogen electrode pressure [1].

A further improvement of the methodology illustrated in [1] is here proposed by leveraging the strength of both UNISA lumped models and UNIGE 2D model (Section II). This allows to perform an advanced estimation of degradation rate according to the following tasks.
The key objective leading to this improvement is related to the need for bringing into the lumped parameter model (that is basically a 0D model) the information related to the spatial distribution of the key parameters within the cell structure and area (information derived by a 2D model, but not available in a 0D approach). Therefore, the UNISA lumped model presented in Section III.1 is improved with information related to parameter surface distribution available in the UNIGE model, without losing the low computational efforts of the lumped model.
The information that can be obtained in this context from the UNIGE 2D model simulation could be, for instance, related to the area distribution of the cell temperature and hydrogen molar fraction, as shown in Figure III.5. The proposed area distributions have been achieved through the simulation of fuel cell with an inlet temperature of 1023 K, a current density of 0.5 A/cm^2 and an inlet H_2 molar fraction of 0.8. From these distributions, minimum, maximum, mean and standard deviation values can be obtained (as also reported in the bottom of Figure III.5). These values can represent a significant improvement in degradation rate estimation, since a distribution range of operating values can be used in the UNISA lumped model. In this way, also degradation effects not affecting the average values but surface distribution instead will be accounted. For instance, local temperature hot spots might introduce a slight increase in the cell temperature average distribution, but they could induce a strong change in the maximum and standard deviation values.

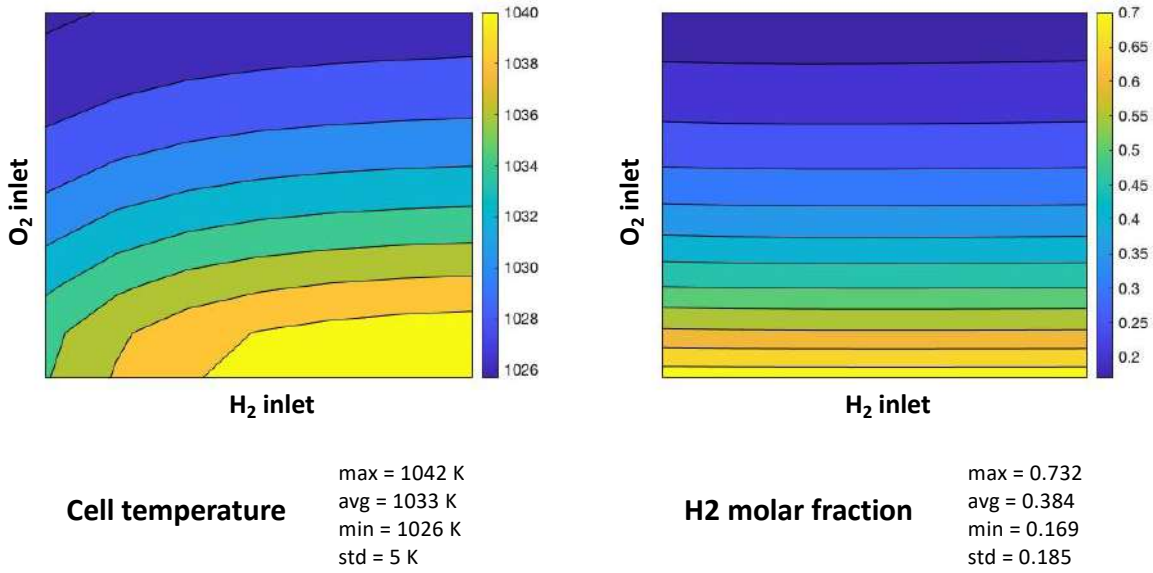

Figure III.5 Area distribution of SOC temperature (left) and H_2 molar fraction (right) simulated by the UNIGE 2D model under crossflow fed fuel cell mode with gas inlet temperature of 1023 K, current density of 0.5 A/cm^2 and inlet H_2 molar fraction of 0.8.

The information related to the parameter distribution embedded within the lumped parameter model can be used to update the methodology for the design of the mathematical transfer functions adding statistical distributions based on physical significance. Specifically, the introduction of such features derived from surface distributions, thus connecting UNISA and UNIGE models, represents the basis of the procedure for the estimation of RUL/degradation rates depicted in Figure III.6.
According to the proposed scheme, the conventional RUL estimation currently performed with the UNISA lumped model is initially shown in Figure III.6-a. This can be easily obtained with the transfer function previously presented (or also with the surface in Figure III.4). In this step, the performance model (or the transfer function itself) is used to simulate the voltage degradation over time, given a degradation phenomenon under a specific operating condition. The RUL is estimated when the voltage reaches the End-of-Life (EOL) criterion, i.e., when failure time occurs. The update of the RUL

estimation is achieved through the first step (step 1 in Figure III.6-b) that consists in the introduction of the variable distribution features (i.e., average, minimum, maximum, etc.) derived from the UNIGE 2D model maps within the UNISA lumped model. In this way, a statistical probability range is associated to the RUL estimation, leading to a failure time window instead of a single stochastic value. The second step (step 2 in Figure III.6-c) can be performed – although not essential in a preliminary analysis – to update the simulation carried out by the UNISA model. In this case, a simulation update time is chosen, and the variable surface distributions are updated with the UNIGE model results. This latter can take as inputs the inlet variables and structural parameters available from the UNISA model (affected by degradation and changed over time) to reduce computational efforts characterising higher-level model dynamic simulation. The updated distribution is then introduced into the UNISA lumped model and the failure time window is updated. As said, this latter step could further improve the estimation of degradation rate and the building of more accurate mathematical transfer functions (since the correlation among degradation rates and accelerating factors is improved through discussed two-step simulation approach).

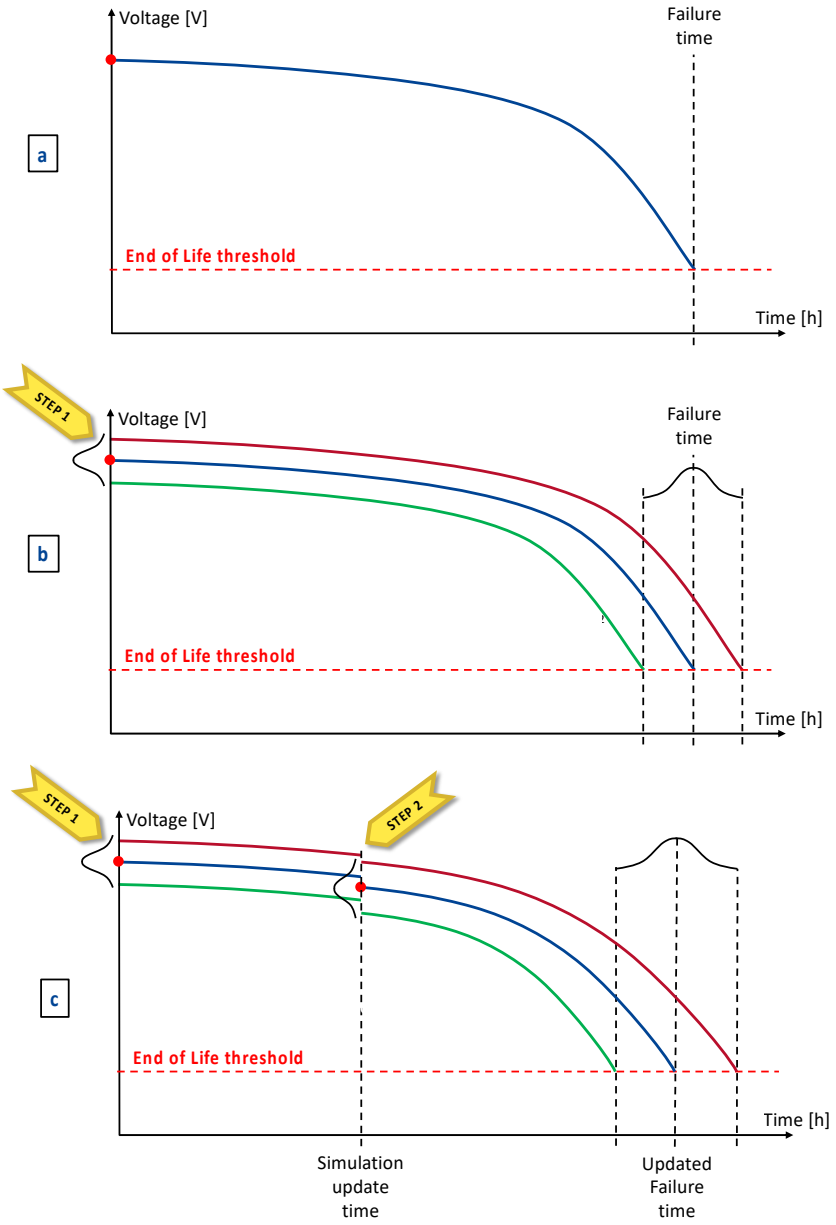

Figure III.6 (a) Initial approach and (b-c) two-steps procedure scheme for degradation rate/RUL estimation combining UNISA lumped model and UNIGE 2D model, useful for the update of mathematical transfer function with embedded statistical significance of accelerating factors.

REFERENCES

[1] P. Polverino, M. Gallo, C. Pianese. Development of mathematical transfer functions correlating Solid Oxide Fuel Cell degradation to operating conditions for Accelerated Stress Test protocols design. Journal of Power Sources, 491, 2021, 229521.

[2] M. Hubert, J. Laurencin, P. Cloetens, B. Morel, D. Montinaro, F. Lefebvre-Joud. Impact of Nickel agglomeration on Solid Oxide Cell operation in fuel cell and electrolysis modes. Journal of Power Sources, 397, 2018, 240-251.

[3] F. Monaco, M. Hubert, J. Vulliet, J. Ouweltjes, D. Montinaro, P. Cloetens, P. Piccardo, F. Lefebvre-Joud, J. Laurencin. Degradation of Ni-YSZ Electrodes in Solid Oxide Cells: Impact of Polarization and Initial Microstructure on the Ni Evolution. Journal of the Electrochemical Society, 166, 2019, F1229.

[4] E. Effori, J. Laurencin, E. da Rosa Silva, M. Hubert, T. David, M. Petitjean, G. Geneste, L. Dessemond, E. Siebert. An elementary kinetic model for the LSCF and LSCF-CGO electrodes of solid oxide cells: impact of operating conditions and degradation on the electrode response. Journal of the Electrochemical Society, 168, 2021, 004520.

[5] J. Laurencin, M. Hubert, D. Ferreira Sanchez, S. Pylypko, M. Morales, A. Morata, B. Morel, D. Montinaro, F. Lefebvre-Joude, E. Siebert. Degradation mechanism of $La_{0.6}Sr_{0.4}Co_{0.2}Fe_{0.8}O_{3-\delta}/Gd_{0.1}Ce_{2-\delta}$ composite electrode operated under solid oxide electrolysis and fuel cell conditions. Electrochimica Acta, 241, 2015, 459-476.

[6] S.P. Jiang. Development of lanthanum strontium cobalt ferrite perovskite electrodes of solid oxide fuel cells – A review. International Journal of Hydrogen Energy, 44, 2019, 7448-7493.

IV. Signal based learning multiple model for cell prognosis (EIFER)

The multiple model algorithm uses a complex structure, which is presented in Figure IV.1. A dataset is provided to a supervisor model, which separates the output data according to operation points or operation intervals of the electrochemical device, as the electrolysis stack in one of the studied cases. The current is used as input parameter to identify the operation points and the voltage is used as output parameter to estimate the degradation. Since there are no physical structures in this model, it is not a problem to exchange the input and output parameters with other system variables based on the operation regime, e.g., constant current or constant power. The voltage could be exchanged with the temperature or there could be even another ageing criteria calculated.

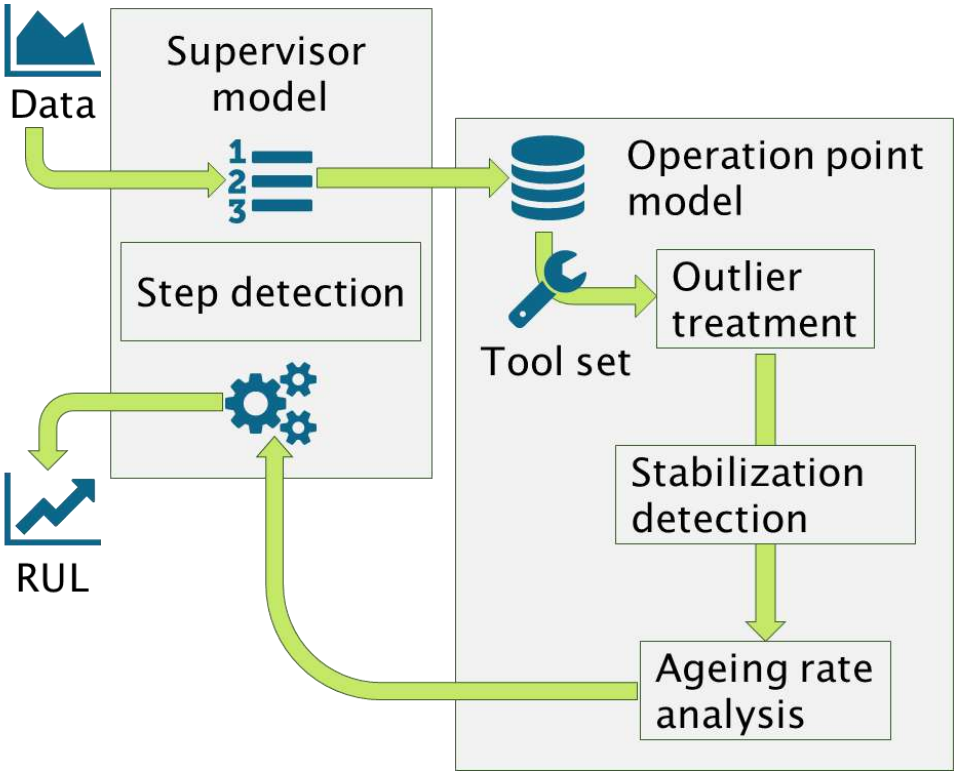

Figure IV.1 Multiple model algorithm.

A calibration phase is used to calculate thresholds and general signal properties.
The supervisor model monitors the sorted data to detect steps and peaks due to possible incidents during the operation. An incident in the data triggers an analysis in the operation point model to clarify if there is a change in the present status or an increased ageing rate. If the data stabilizes again at comparable values and rates like before the incident, the old database is kept and will be used. If there are significant changes, the old data is kept but not used any longer for prognosis. The change is quantified and reported to the operator.
Each operation point model has its operation point related data and a toolbox with different methods, which can even include evaluation method to decide among different fitting functions in order to detect the best fit for the future. Outliers should not be considered since they are more related to the measurement system than to the monitored stack. Consequently, the approach is to detect and replace them by mean values based on the former data points. A key information is to evaluate the stability of the data. Short-term dynamics have much bigger impacts on the voltage than the ageing rate. Therefore, the dynamic processes make a feasible estimation of the long-term operation very difficult. The ageing rate and the present status should be analysed on the stabilized parts. There could be an analysis to detect the source of instabilities, but from a systematic point of view it is more

important to compare and analyse data that has a comparable stability. Prognosis requires data that was measured under the same or similar conditions in order to identify the degradation based on the same system status. If the data is very dynamic, a time analysing method to find transitional time delays is more preferable than a linear fit for the ageing analysis. Last but not least a suitable ageing parameter is used for estimation and is provided to the supervisor model.
In the end, the supervisor model uses the information of all operation point models and the most probable future load profile based on the input parameter to estimate the decrease in the output parameter usually until a deterioration of 20 %.
The proof of concept for the multiple model algorithm was already done for PEM fuel cells [1]. Since the subject is very complex, an important goal during the project was a proof of concept for solid oxide cells and the improvement of key methods, like the step detection, the stabilization detection and the online outlier treatment. If the methods work in a proper way, they provide analysis results like in the next sections.

IV.1 Analysis on data measured by EIFER

First measurement series

Figure IV.2 and Figure IV.3 present different operation points (26 A and -64 A as applied currents) of the electrolyte supported 10 cell stacks (Ni-GDC/GDC/3YSZ/GDC/LSCF). All figures plot the voltage in volt as function of the time in hours. The top plots present the overview over the complete measurement series. The title of the top plots includes estimations of the Remaining Useful Lifetime (RUL) in years for the different parts until computing a voltage reduction of 20 %. When the current is 0 A, it is not considered as operation and therefore has no RUL estimation. The bottom plots are zoomed in views of the fitted data. The stabilized parts and the fits are coloured. In addition, the title of the bottom plots presents the voltage means and the ageing rates as well to support any analysis of the experiments.

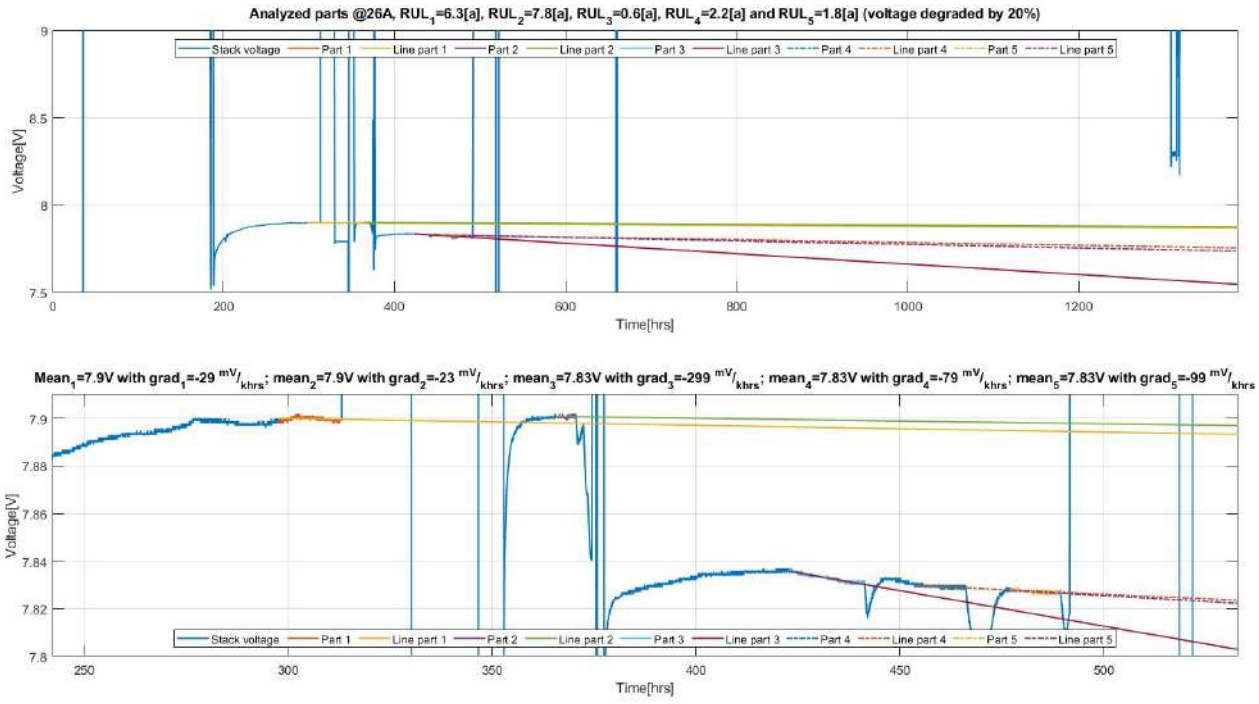

Figure IV.2 First dataset focused on a current of 26 A (fuel cell mode).

Figure IV.2 presents a decreasing voltage in all presented windows, which is consistent since the stack runs in fuel cell mode. The stack runs well until 370 hours. The mean values and the ageing rates before this time are similar, even if there are some other events in between. The first part of

Figure IV.2 can be taken as showcase to explain how systematic prognosis acutally works. Unfortuantely, it seems that an incident takes place after 370 hours. The degradation analysis makes it possible to quantify a 10 % loss of voltage due to the incident. In addition, the ageing rate increases as well, but seems to stabilize around 450 hours at a higher degradation with respect to the values before the incident. The observations are supported by the RUL estimations of the different fits.

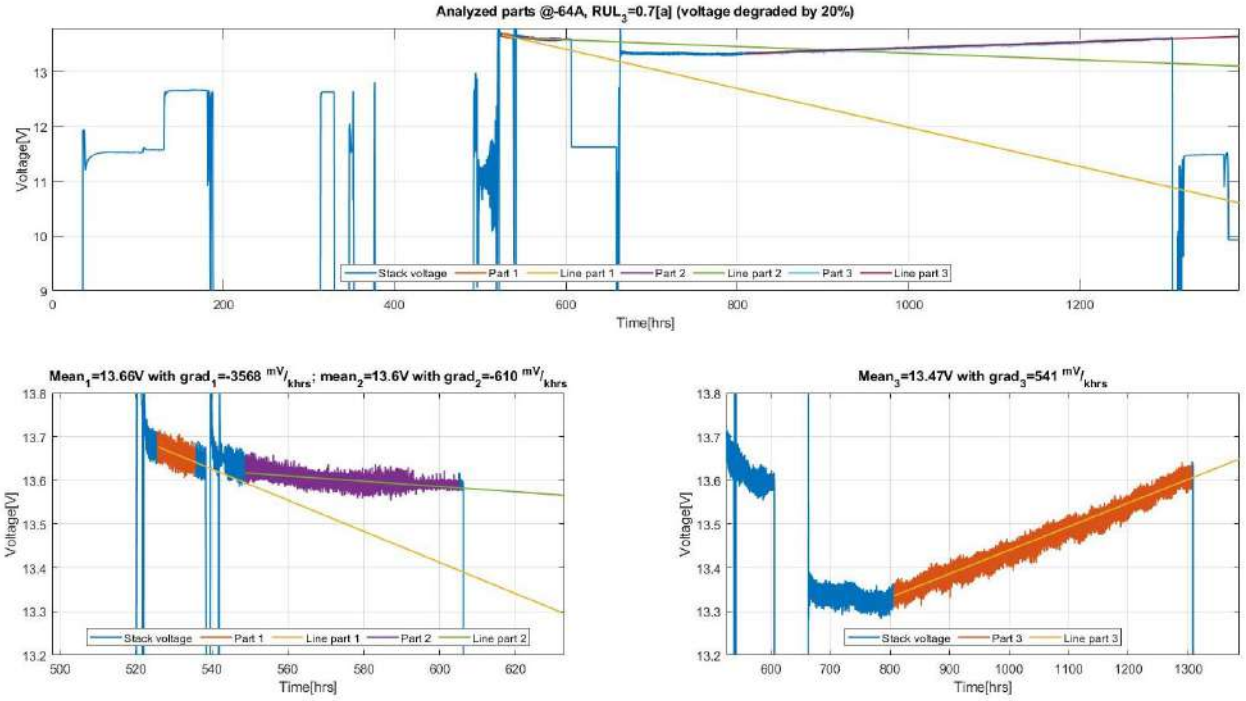

Figure IV.3 First dataset focused on a current of -64 A (electrolysis mode).

Figure IV.3 shows the stack working at -64 A in electrolysis mode. The bottom left graph presents a decreasing voltage between 500-600 hours, which is not the expected behaviour for electrolysis mode. Most probably, it did not reach a stabilized equilibrium yet. Whereas the bottom right plot shows the expected behaviour: an increasing voltage during electrolysis mode after 700 hours. It starts at lower voltage compared to the bottom left graph. Unfortunately, the degradation is quite significant and it does not take long to reach a 20 % decrease in the voltage, which is support by a RUL estimation of 0.7 year. According to the log from the lab, the evaporator was close to its end of life. The effect on the stack was devastating and urges to implement a condition monitoring with a condition-based maintenance approach. The incident underlines the need for advanced maintenance techniques, since a significant degradation of a stack is not necessarily caused by the stack but be due to the balance of plant and its components.

Second measurement series

Figure IV.4 shows longer stabilization phases at -64 A electrolysis mode and a short operation at -60 A. After 850 hours, the trend stabilizes and turns to an increasing voltage which is expected for electrolysis mode.

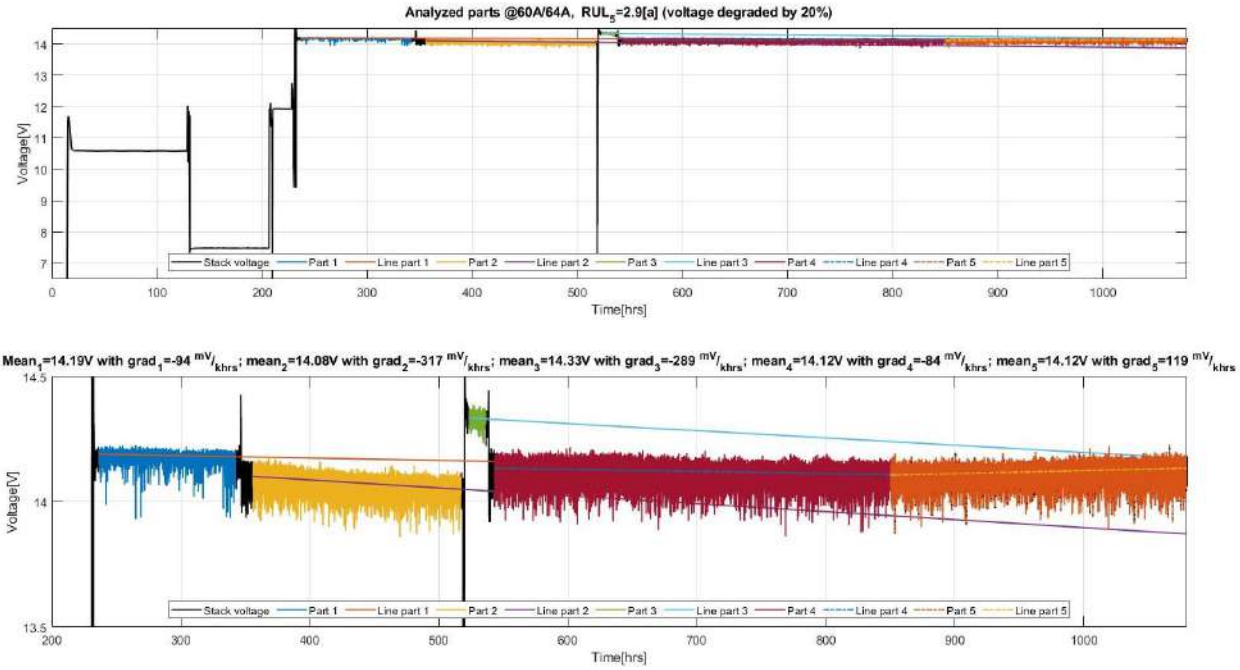

Figure IV.4 Second dataset focused on a current of -60 A and -64 A (electrolysis mode).

Table IV.1 provides an overview of the two-measurement series considering all different applied operation points. It can be concluded from the time basis of the stabilized operation hours that the second measurement series went better after the evaporator was replaced in comparison to the first one. In addition, the RUL estimation of the fuel cell mode of 2.6 years and the electrolysis mode of 2.9 years are comparable in this last dataset.

Table IV.1 Ageing rates related to two measured datasets with their basis in hrs.

	1st				2nd			
Current [A]	Mean [V]	Rate [mV per khrs]	RUL [d]	Basis [hrs]	Mean [V]	Rate [mV per khrs]	RUL [d]	Basis [hrs]
0A	12.66 12.67 11.49	-132 -434 116	- - -	15 16 25	10.59 11.93	-55 -276	- -	103 16
26A	7.9 7.9 7.83 7.83 7.83	-29 -23 -299 -79 -99	2305 2862 229 815 652	14 4 18 12 12	7.49	-67	1001	50
-60A -64A	 13.66 13.6 13.47	 -3568 -610 541	 - - 251	 9 57 496	14.19 14.08 14.33 14.12 14.12	-94 -317 -289 -84 119	- - - - 1119	105 162 15 306 260

Outlier treatment

As an important step for cell operation analysis, an outlier treatment was developed. It is based on the last values and the double standard deviation. The standard deviation and the mean values are calculated based on the last measured values. If the threshold of double standard deviation plus the mean value is crossed, the next measured point is analysed as well. If the next value is within the last value plus the double standard variation, a peak or a step is likely. Otherwise, an outlier is likely and the last value will be corrected by its neighbour values.

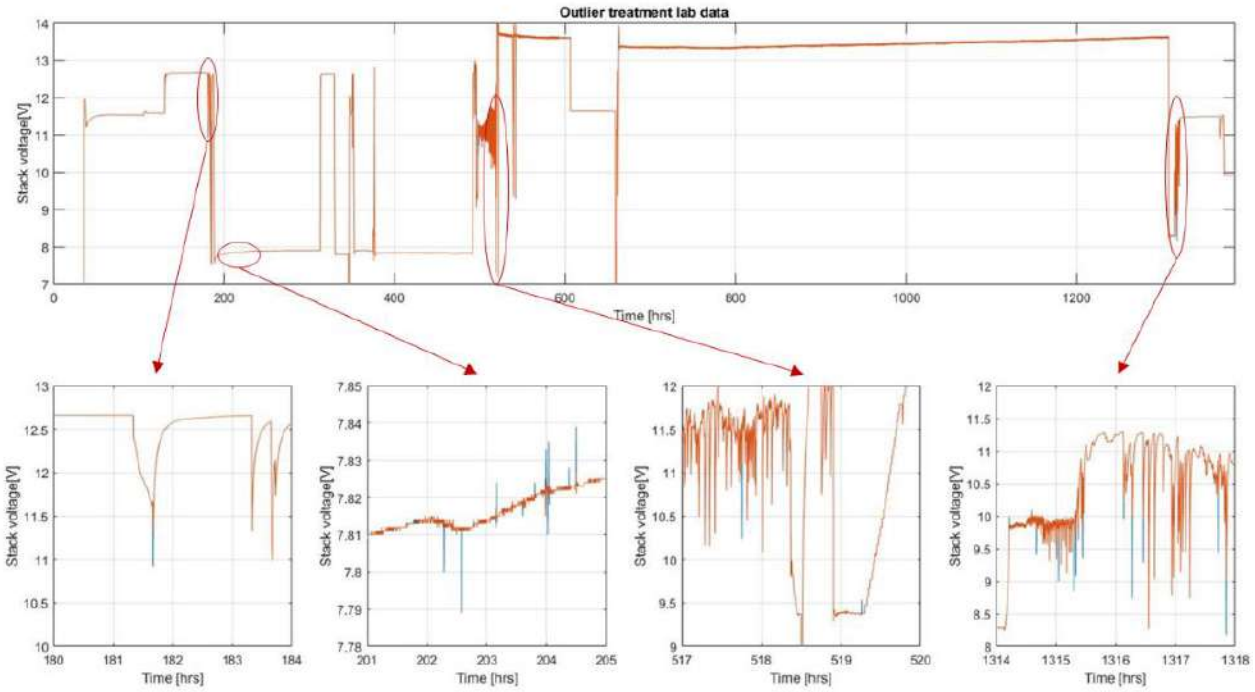

Figure IV.5 First dataset where blue represents the untreated data and red the treated data. The four plots on the bottom show examples to prove that the treatment deleted single values but kept ramps and steps.

The window of the double standard deviation includes over 100 past values to reduce the impact of steps on the outlier treatment. The treatment was successfully tested on the initial and the first measured dataset. Figure IV.5 shows the results. The first measured dataset shows not so much noise; therefore, it was not corrected many times. It is important to notice that noise based on a less stable operation was not corrected, since it is related to real observed system behaviour and not outliers.

IV.2 Analysis on data shared within AD ASTRA consortium

In order to challenge and show the capabilities the algorithm, the following data of partners were investigated:

- CEA data set 1 - “CEA_data 15m Elisa3 8pC_steam in air”, air humidified at 8% - ΔU = 45 mV/kh (12 mV/kh after 600 h of operation);
- CEA data set 2 - “CEA_data collées 15min L717”, dry air - ΔU = 27 mV/kh (7 mV/kh after 600 h of operation);
- CEA data set 3 - “CEA_data collées 15min L718 sofc”, fuel cell mode - air humidified at 8% - ΔU = 20 mV/kh;
- DTU data set 1 - “DTU_12test138_durability” and DTU data set 2 - “ESC_6test79_V_t 96_4 H2 H2O_1000h”;
- EPFL data set 1 - “0042_EPFL_New_V-t_2021426124144” and EPFL data set 2 - “UvsTime_0040_2021426124951”.

A key step for the proposed approach is the automated operation point detection in order to sort data according to comparable operation states. Figure IV.6, Figure IV.7 and Figure IV.8 show the results for some of the partners’ data. The top plot presents the main parameter, which was used for sorting the data according to the operation points of the chosen parameter. It can be the current like in

Figure IV.8 or any other system parameter as well; e.g. Figure IV.6 was classified based on the temperature and Figure IV.7 was classified based on the oxygen. The different operation points are coloured to visualize the results. The middle and the bottom plot show other system parameters, which are classified into zones based on the top parameter. Figure IV.8 shows the sectioning based on the current, but it shows as well an incident in the voltage. The incident has to be identified by the step detection and needs to be investigated since the main operation parameter did not change, but a core output parameter is disturbed. This data should not be used for prognosis neither, because it represents a nonnominal operation which might lead to a nonnominal degradation. The algorithm needs to detect if the disturbance stabilizes or if it is reversed and the system comes back to its old state. This might sound trivial for a single operation point, but if there are two or more parameters selected as main parameters, an automated detection and organisation of operation point models can handle different data sets and provide a reliable prognosis and a diagnosis on top.

In addition, Figure IV.6 and Figure IV.7 show the potential to use different operation parameters beside the current as the main operation point. It is possible to develop the algorithm towards a multidimensional matrix. Instead of using one operation point parameter to create databases with similar operation states, two or three operation parameters could be used, forming matrices of operation point models. On the other hand, a future operation profile of each operation parameter is required as well in this case.

Figure IV.6 presents the data classified by the parameter “Coclyco1T1” (i.e., the temperature) under almost constant current (not plotted). “Coclyco1U1” is the voltage and “Coclyco1RDM_O2” is related to the flow rate of oxygen. Due to the automatic classification, the impact of “Coclyco1T1” can be analysed. It seems to speed up the degradation. After 1200 hours, the current is switched off for a while, which leads somehow to an improved performance. On the other hand, at 1500 hours, the trend before 1200 hours is reached again. “Coclyco1RDM_O2” has a more significant impact on the voltage than “Coclyco1T1” and can be clearly detected.

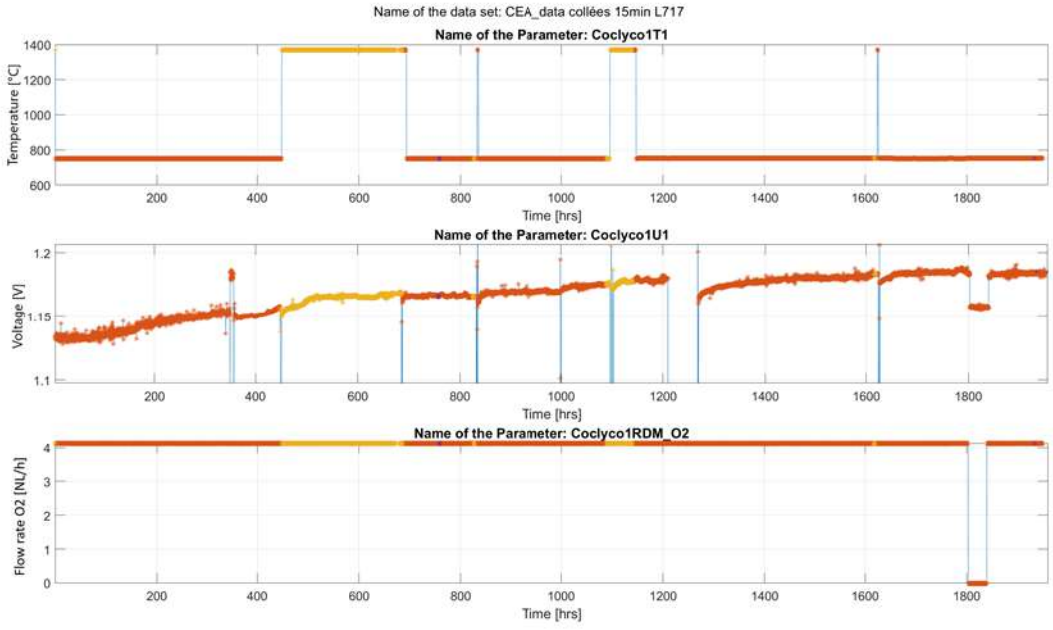

Figure IV.6 CEA data investigated by the Coclyco1T1 as main operation parameter.

Figure IV.7 shows the impact of “O2_in”. “O2_in” is the Nernst potential between the fuel gas in and (outer) air in the sensor. The peaks are caused by the current. In this case it would make sense to use both, the current and “O2_in” as main operation point parameters. “O2_in” shows a clear relation the voltage.

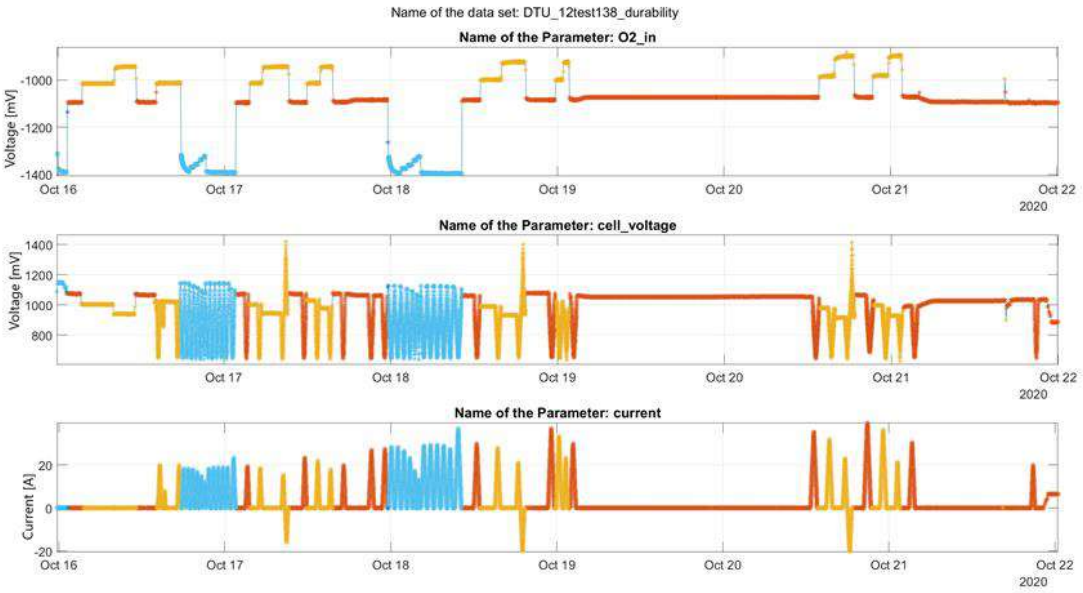

Figure IV.7 DTU investigated by different O2_in as main operation parameter.

Figure IV.8 presents the current as main operation parameter, which is the common approach for operating electrochemical devices. In addition, an incident around 500 hours is included in this dataset as well. The algorithm sorts the data to the operation points and the operation point model analyses its dataset. In this case, the incident causes instability and a step which is detected by the algorithm. An incident might change the state of the cell or stack in a way that it ages faster or loses some lifetime. As a conclusion, the algorithm has to monitor and to analyse the new state but keep the old state in case a reversible effect happened. Another important aspect is that the algorithm should only include stabilized parts of the data to prognose the lifetime. Therefore, the Sum of Absolute Difference (SAD) based on a moving averaged was applied as described in the followed section.

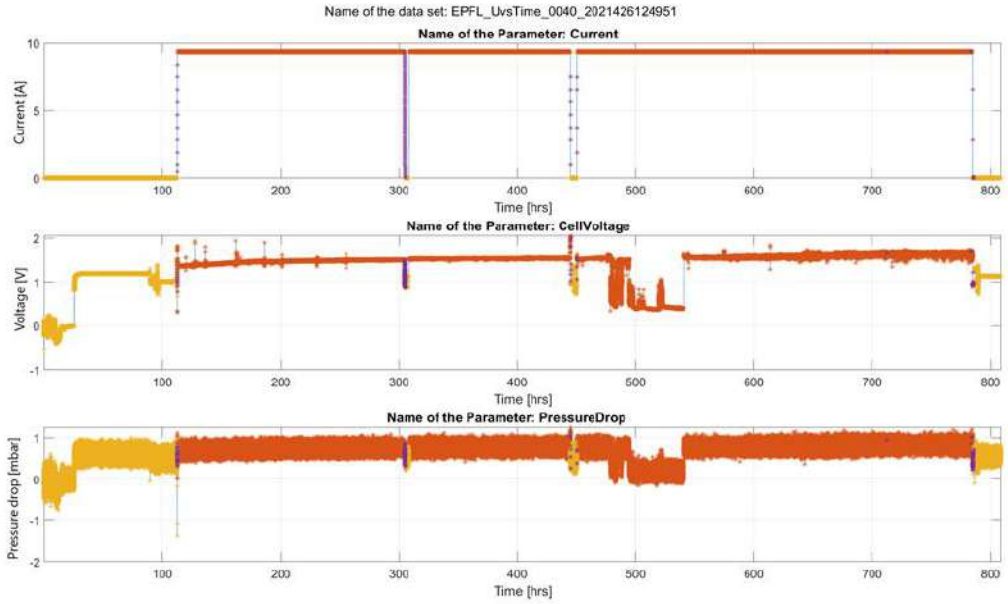

Figure IV.8 EPFL data investigated by current as operation parameter. The pressure drop sensor shows some capabilities to detect the occurred incident at 500 h and may be some potential for diagnosis as well.

Step detection and stabilisation detection

The Sum of Absolute Difference (SAD) is applied on a 100 values window for analysing the present data. The moving mean is calculated for different sizes of the moving window. The bigger the window gets, the smaller the SAD between the moving averaged and the original data is, when the signal is stable. The change of the SAD (ΔSAD) shows a comparable picture if there are no local disturbance. Local disturbances are for example fluctuations or significant oscillations. The changed is normalized based on its maximum. If a step occurs, the first value is not any longer the maximum value.
The method was applied on EPFL data presented in Figure IV.8. The incident around 500 hours was taken as example to show the capabilities of the approach. Figure IV.9 and Figure IV.10 present the results related to parts before the incident and Figure IV.11 shows the incident.

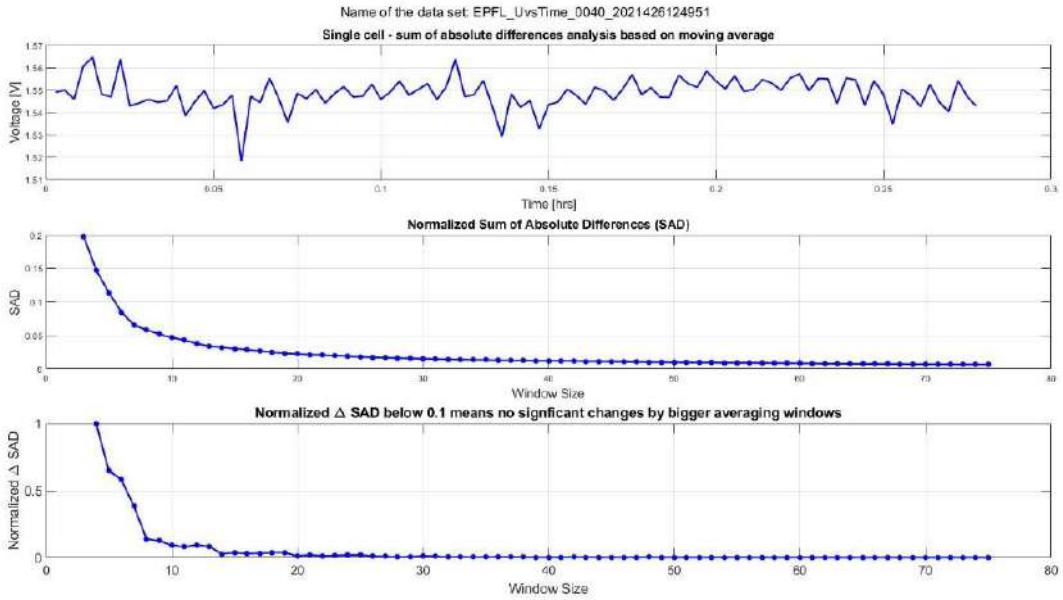

Figure IV.9 Stabilized voltage signal (top) - Sum of Absolute Difference (SAD) between the stabilized signal and the moving mean with different window sizes (middle) - Normalized change of the SAD (ΔSAD) (bottom).

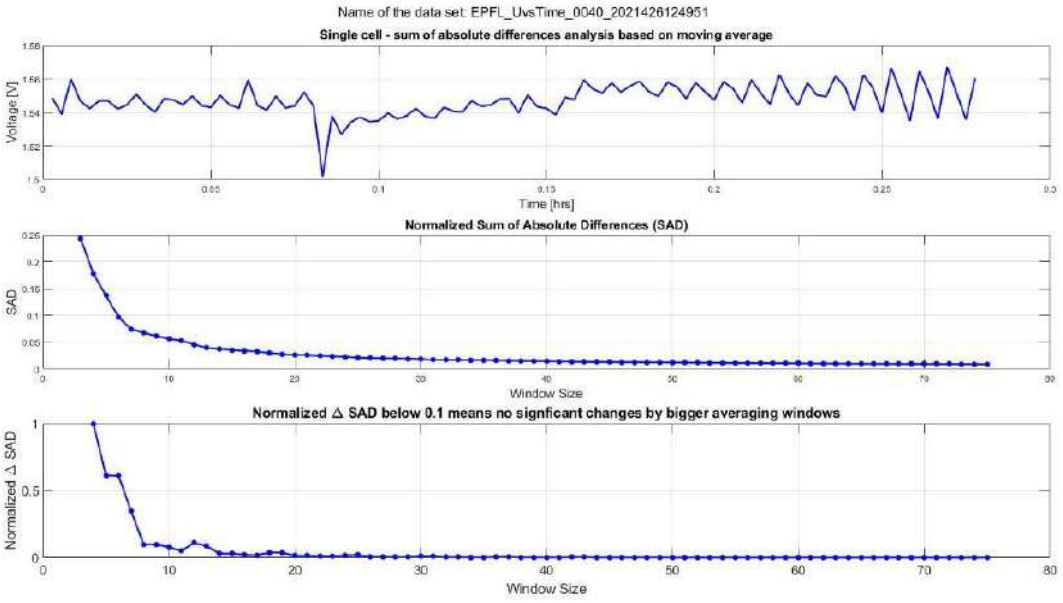

Figure IV.10 Locally disturbed voltage signal (top) - Sum of Absolute Difference (SAD) between the voltage signal and the moving mean with different window sizes (middle) - Normalized change of the SAD (ΔSAD) with a folded trend (bottom).

Figure IV.9 shows a stabilized part of the data. The SAD and the normalized ΔSAD show a more or less asymptotic and orderly trend. The more unstable the part of the data gets, the more chaotic both criteria become. Figure IV.10 shows a disturbed trend in ΔSAD, which can be noticed in the plotted part of the voltage signal. The voltage signal of Figure IV.10 is more chaotic and irregular than the voltage signal of Figure IV.9.

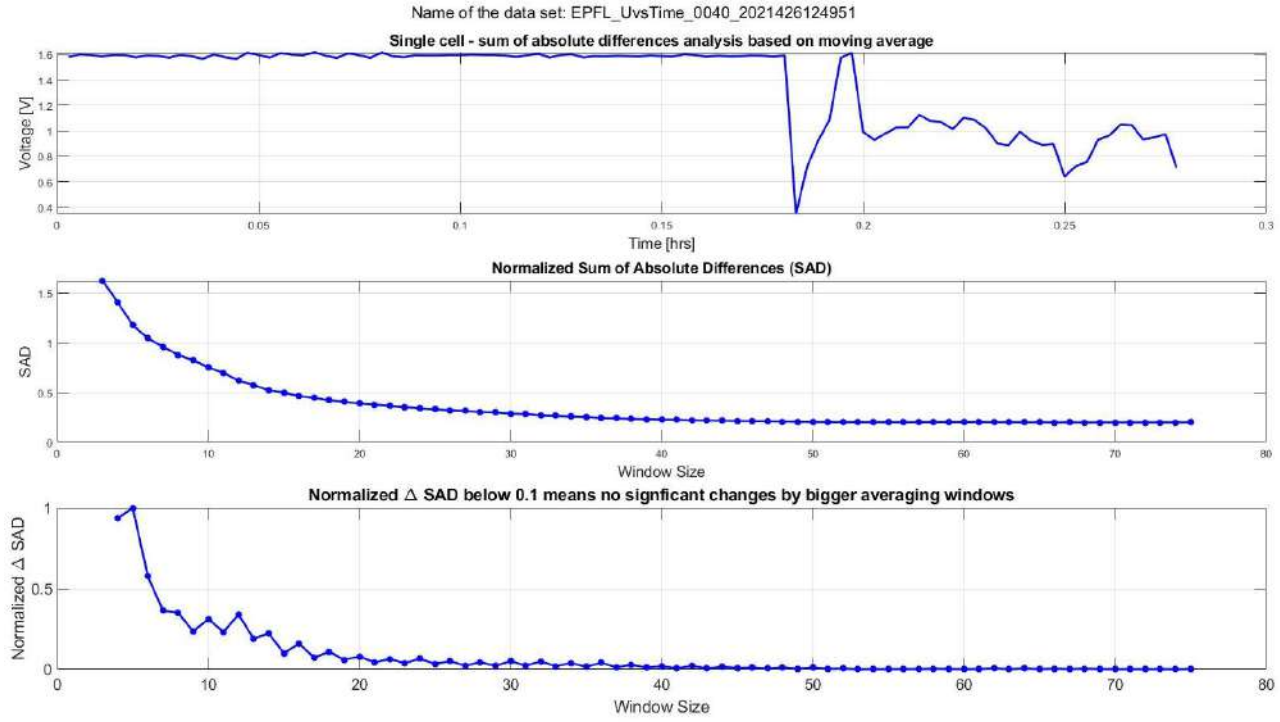

Figure IV.11 Voltage signal with a noisy step (top) - Sum of Absolute Difference (SAD) between the voltage signal and the moving mean with different window sizes (middle) - Normalized change of the SAD (ΔSAD) with a disarranged maximum value (bottom).

Figure IV.11 presents the voltage trend with a noisy but significant step. As a consequence, ΔSAD breaks the asymptotic trend completely by changing the position of the maximum value and saw tooth shape of the trend. In some cases, the SAD is more suited to detect steps and both criteria are impacted by constant values as well. The stabilisation detection is challenging, especially if a general approach is desired. Different types of noise, different signals to noise ratios and differently measured data usually need to be investigated individually. The found approach was successfully used on previously shown data, but more validation on different systems is recommended to investigate the robustness of the criteria.

Ageing rate investigation

The ageing rate investigation of EPFL sample is represented in Figure IV.12. The plot visualizes that at 200 hours some useful changes were made since the degradation rate reduces significant and the voltage is in the beginning even lower than values before 200 hours. The shut down around 300 hours reduces the ageing rate even further, but voltage increases by several percent, which means a sudden consumption of lifetime for a small degradation rate. The incident around 450 hours leads to significant increased degradation rates, even afterwards at 550 hours when the cell was recovered from the incident. On the other hand, the voltage does not change much. There is no sudden consumption of lifetime during this incident. Starting from 700 hours, the cell is stabilized again and degrades under a small rate.

The results of the aging analysis for all EPFL data is plotted in Table IV.2. Table IV.3, Table IV.4 and Table IV.5 present the analysis results for all DTU and CEA data sets. If the mean voltage in Table IV.2 decreases due to an incident, in most of the cases the ageing rate increases significant for a while. In SOEC mode, a decrease of the voltage means an improvement of the performance under constant current.

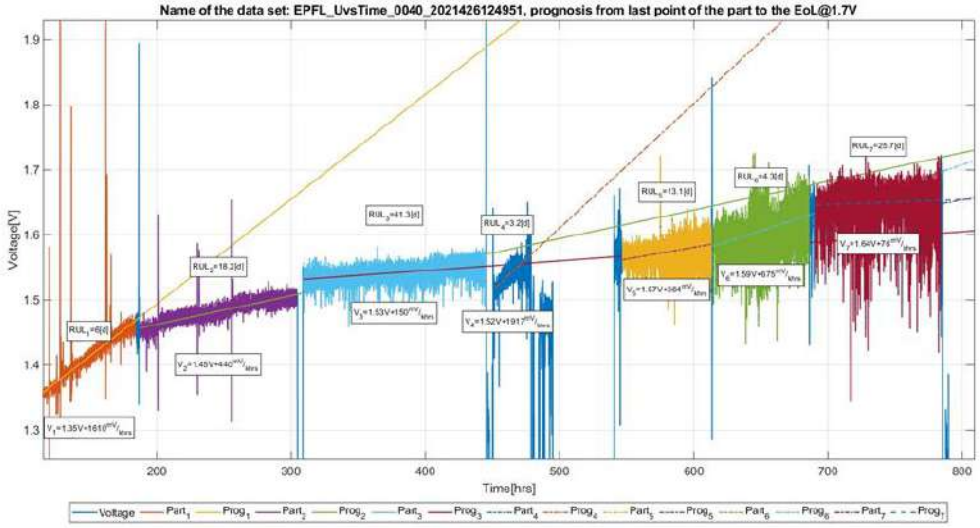

Figure IV.12 Remaining useful lifetime estimation of "UvsTime_0040_2021426124951" dataset from EPFL sample with mean₁=1.41 V and grad₁=1610 mV per khrs; mean₂=1.48 V and grad₂=440 mV per khrs; mean₃=1.54 V and grad₃=150 mV per khrs; mean₄=1.54 V and grad₄=1917 mV per khrs; mean₅=1.57 V and grad₅=364 mV per khrs; mean₆=1.61 V and grad₆=675 mV per khrs; mean₇=1.65 V with grad₇=76 mV per khrs.

Table IV.2 Ageing rates related to the measured datasets with their basis in hrs for EPFL data in SOEC mode.

	EPFL_EPFL_New_V-t_2021426124144					EPFL_UvsTime_0040_20214 26124951			
Current [A]	Mean [V]	Rate [mV per khrs]	RUL [d]	Basis [hrs]	Current [A]	Mean [V]	Rate [mV per khrs]	RUL [d]	Basis [hrs]
-10A	1.17	1584	8	74	-9.37 A	1.35	1610	6	69
	1.32	763	12	83		1.45	440	18	116
	1.39	680	10	77		1.53	150	41	136
	1.45	557	11	22		1.52	1917	3	19
	1.37	2270	4	15		1.57	364	4	66
	1.36	939	7	68		1.59	675	26	71
	1.44	428	15	27		1.64	76		93
	1.45	324	15	90					
	1.49	268	14	69					
	1.51	254	11	66					

Figure IV.13 and Figure IV.14 show the ageing analysis regarding data from DTU and CEA, respectively. For the first case, the continuous galvanostatic operation in Figure IV.13 starts at around 200 hours and shows a stable phase until 375 hours. Afterwards, the experiment includes significant fluctuations. The trend regenerates and reaches at 500 hours the value from the beginning. After 600 hours, it starts to degrade more significant with comparable degradation rates, intermitted by phases of regeneration. At around 1150 hours, the degradation accelerates again and keeps its highest value until the end of the continuous galvanostatic operation. Table IV.3 shows the results for the DTU data.

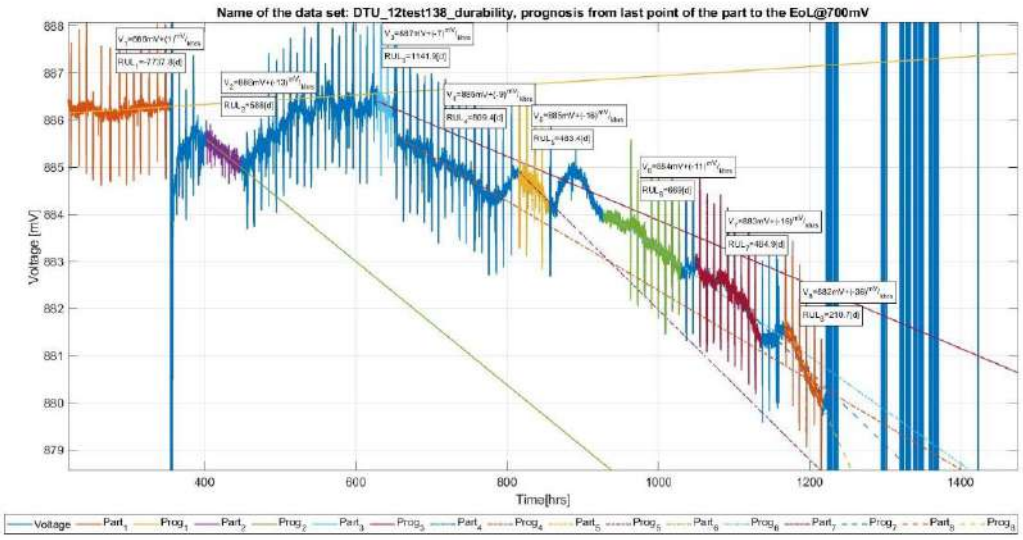

Figure IV.13 Remaining useful lifetime estimations of "DTU_12test138_durability" dataset from DTU with ageing rates and voltages after significant changes of the state.

Table IV.3 Ageing rates related to the measured datasets with their basis in hrs for DTU data in SOFC mode.

	DTU_12test138_durability					DTU_ESC_6test79_V_t 96_4 H2 H2O_1000h			
Current [A]	Mean [mV]	Rate [mV per khrs]	RUL [d]	Basis [hrs]	Current [A]	Mean [mV]	Rate [mV per khrs]	RUL [d]	Basis [hrs]
6,41A	886	1	-	138	3,18 A	931	-81	14	34
	886	-13	588	45		923	-36	26	34
	887	-7	1142	21		921	-13	65	42
	885	-9	809	123		918	-1	699	56
	885	-16	483	41		918	-10	69	109
	884	-11	669	104		917	-5	145	72
	883	-16	485	88		917	-4	158	214
	882	-36	210	52		916	-2	353	97
						916	-12	46	208

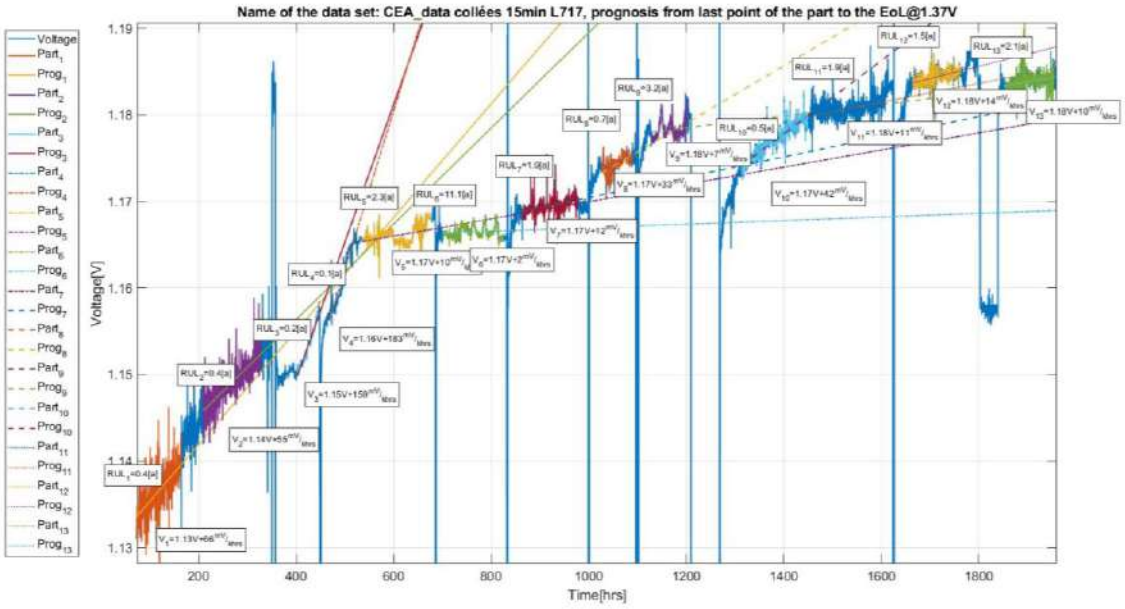

Figure IV.14 Remaining useful lifetime estimations of "CEA_data collées 15min L717" dataset from CEA with ageing rates and voltages after incidents.

Figure IV.14 shows a kind of “formation phase” until 500 hours, which can be noticed by the prognosed trends despite that there is some regeneration with a follow up of high ageing rates at 400 hours. The prognosed trends $Prog_5$, $Prog_7$ and $Prog_9$ give good estimations for the followed trends $Part_{11}$, $Part_{12}$ and $Part_{13}$. $Part_6$ seems to run under very favourable conditions and $Part_{10}$ shows an adaptation of the voltage towards its stabilized state. Table IV.4 adds an interesting aspect to the analysis. Whenever the voltage decreases significant below its last stable value, the ageing rate increases significant to somehow come back to a former trend. The significant increased ageing rate causes a decreased remaining useful lifetime. Table IV.5 shows the results for SOFC mode.

Table IV.4 Ageing rates related to the measured datasets with their basis in hrs for CEA data in SOEC mode.

	CEA_data 15m Elisa3 8pC_steam in air					CEA_data collées 15min L717			
Current [A]	Mean [V]	Rate [mV per khrs]	RUL [d]	Basis [hrs]	Current [A]	Mean [V]	Rate [mV per khrs]	RUL [d]	Basis [hrs]
-6,78 A	1.17	107	88	98	-6,78 A	1.13	66	0.4	91
	1.18	97	78	481		1.14	55	0.4	118
	1.22	96	77	34		1.15	159	0.2	43
	1.22	78	88	257		1.16	183	0.1	56
	1.24	14	498	60		1.17	10	2.3	140
	1.24	103	63	77		1.17	2	11.1	126
	1.25	17	374	509		1.17	12	1.9	113
	1.25	-21	-	220		1.17	33	0.7	63
						1.18	7	3.2	72
						1.17	42	0.5	136
						1.18	11	1.9	142
						1.18	14	1.5	99
						1.18	10	2.1	102

Table IV.5 Ageing rates related to the measured datasets with their basis in hrs for CEA data in SOFC mode.

	CEA_data collées 15min L718 sofc			
Current [A]	Mean [V]	Rate [mV per khrs]	RUL [d]	Basis [hrs]
6,72 A	0.81	-25	258	425
	0.8	-32	189	215
	0.8	-21	265	622
	0.78	-48	101	245
	0.77	-30	156	140

All the data seem to include an initial formation process when the continuous operation is started. After several 100 hours the effective degradation trends establish, which appears kind of similar in degradation rates and prognosing the future trends in an acceptable way. Even if some incidents cause fluctuations of the voltage trends, the experimental profiles tend to stabilize towards prognosed fits of the past. Understanding the reasons of the fluctuations, which displace the voltages in a positive or a negative way from the prognosed trends, could be helpful for improving the performance.

To conclude, the proposed signal-based learning multiple model for cell prognosis was validated on different sets of data acquired during the project Ad Astra. In addition, some methods for full-automated black box model approach were developed. The automated operation point detection, the online outlier treatment, the step detection and the stability detection are core elements to achieve this long-term goal. Thanks to the general approach, the algorithm can develop further on other data and other systems. One required step would be to combine all methods in one big algorithm, which could not be achieved yet. The methods are still applied in a sequential way. Another recommended action is the validation of the developed methods on other systems and data to ensure their robustness versus changing conditions of measurements and control systems.

REFERENCES

[1] E. Lechartier, C. Kändler. D6.2: Tests and performance evaluation of prognostic approaches. SAPPHIRE - System Automation of PEMFCs with Prognostics and Health management for Improved Reliability and Economy (325275). 2016. https://doi.org/10.5281/zenodo.1199275.